Non-invasive Retrieval of the Transmission Matrix for Optical Imaging Deep Inside a Multiple Scattering Medium

Ulysse Najar, Victor Barolle, Paul Balondrade, Mathias Fink, A Claude Boccara, Alexandre Aubry

Non-invasive Retrieval of the Transmission Matrix for Optical Imaging Deep Inside a Multiple Scattering Medium

Ulysse Najar, Victor Barolle, Paul Balondrade,
Mathias Fink, A. Claude Boccara, and Alexandre Aubry
Institut Langevin, ESPCI Paris, PSL University, CNRS, Paris, France

(Dated: February 10, 2023)

Abstract

As light travels through a disordered medium such as biological tissues, it undergoes multiple scattering events. This phenomenon is detrimental to in-depth optical microscopy, as it causes a drastic degradation of contrast, resolution and brightness of the resulting image beyond a few scattering mean free paths. However, the information about the inner reflectivity of the sample is not lost; only scrambled. To recover this information, a matrix approach of optical imaging can be fruitful. Here we report on the compressed measurement of a high-dimension reflection matrix R via low coherence interferometry. Then, we show how the inner transmission matrix linking each camera sensor and each medium voxel can be extracted through an iterative multi-scale analysis of wave distortions contained in R. This transmission matrix is the Holy Grail for volumetric imaging since it enables an optimal compensation of forward multiple scattering paths and provides a three-dimensional confocal image of the sample as the latter one had become digitally transparent. The proof-of-concept experiment is performed on a human opaque cornea and an extension of the penetration depth by a factor five is demonstrated compared to the state-of-the-art.

Multiple scattering of waves concerns many domains of physics, ranging from optics or acoustics to solid-state physics, seismology, medical imaging, or telecommunications. In an inhomogeneous medium where the refractive index n depends on the spatial coordinates $\mathbf{r}$, several physical parameters are relevant to characterize wave propagation: (i) the scattering mean free path ℓ_s, which is the average distance between two successive scattering events; (ii) the transport mean free path ℓ_t, which is the distance after which the wave has lost the memory of its initial direction. For a penetration depth z smaller than ℓ_s, ballistic light is predominant and standard focusing methods can be employed; for $z > \ell_s$, multiple scattering events result in a gradual randomization of the propagation direction before reaching the diffusive regime for $z > \ell_t$. Although it gives rise to fascinating interference phenomena such as perfect transmission[1,2] or Anderson localization[3,4], multiple scattering still represents a major obstacle to deep imaging and focusing of light inside complex media[5,6].

In the past decades, there have been many proposals for the harnessing of waves through complex media. With the emergence of multi-element technology, wave-fields can be tamed in order to take advantage of the complexity of propagation media to focus waves through them or image objects hidden behind them. This has been be realized in acoustics using the concept of the time reversal mirror or in optics using wave-front shaping techniques[7]. More fundamentally, a matrix formalism is particularly appropriate in wave physics[8,9] when the wave field can be controlled by transmission[10] and/or reception[11] arrays of independent elements.

While a subsequent amount of work has considered the transmission matrix $\mathbf{T}$ for optimizing wave control and focusing through complex media[12–17], this configuration is not the most relevant for imaging purposes since only one side of the medium is accessible for most *in-vivo* applications. Moreover, in all the aforementioned works, the scattering medium is usually considered as a black box, while imaging requires to open it. To that aim, a *reflection matrix approach of wave imaging* (RMI) has been developed for the last few years[18–21]. The objective is to determine, from the reflection matrix $\mathbf{R}$, the $\mathbf{T}$-matrix between sensors outside the medium and voxels mapping the sample[22] (Fig. 1). Previous works have mainly considered the imaging of highly reflecting structures (*e.g* myelin fibers) through an aberrating layer (*e.g* mouse skull)[20], in a wavelength range that limits scattering and aberration from tissues[23]. On the contrary, here, we want to address the extremely challenging case[24] of three-dimensional imaging of biological tissues themselves (cells, collagen,

extracellular matrix etc.) at large penetration depth ($z \sim 5\ell_s$), regime in which aberration and scattering effects are spatially-distributed over multiple length-scales.

In previous studies, coherent measurements of $\mathbf{R}$ have been performed either in a plane wave basis[25], point-to-point basis[20], or between those dual bases[26,27]. In this paper, a low coherence interferometry set up, derived from full-field optical coherence tomography (FFOCT)[28,29], is used to record the $\mathbf{R}-$matrix in a de-scanned basis. Interestingly, this frame drastically reduces the number of input wave-fronts required for a full measurement of $\mathbf{R}$.

Another advantage of this basis is the direct access to the distortion matrix $\mathbf{D}$ through a Fourier transform. This matrix basically connects any focusing point with the distorted part of the associated reflected wavefront[19,21]. A multi-scale analysis of $\mathbf{D}$ is here proposed to estimate the forward scattering component of the $\mathbf{T}$-matrix at an unprecedented spatial resolution ($\sim$6 μm). Once the latter matrix is known, one can actually unscramble, in post-processing, all wave distortions and multiple scattering events undergone by the incident and reflected waves for each voxel. A three-dimensional confocal image of the medium can then be retrieved as if the medium had been made digitally transparent.

The experimental proof-of-concept presented in this paper is performed on a human *ex-vivo* cornea that we chose deliberately to be extremely opaque. Its overall thickness is of 5 ℓ_s. FFOCT shows an imaging depth limit of $1\ell_s$ due to aberration and scattering. Strikingly, RMI enables to recover a full 3D image of the cornea at a resolution close to $\lambda/4$ ($\sim$ 230nm) and a penetration depth enhanced by, at least, a factor five.

Focused Reflection Matrix in De-Scanned Basis

The $\mathbf{R}$-matrix is generally defined as containing responses between a recording basis (camera pixels) and an illumination basis, that corresponds to the set of incident waves used to probe the sample (Fig. 1a). Once recorded, $\mathbf{R}$ can be easily projected by simple matrix products in: (i) the pupil plane ($\mathbf{u}_{\mathrm{in/out}}$) where input-output correlations can be exploited for full-field aberration compensation[20,30]; (ii) the focused basis ($\boldsymbol{\rho}_{\mathrm{in/out}}$) where an image of the sample can be formed. Compared to confocal imaging where focusing is performed at input and output on the same point ($\boldsymbol{\rho}_{\mathrm{in}} = \boldsymbol{\rho}_{\mathrm{out}}$), RMI enables the decoupling of input and output focal spots. Interestingly, the off-diagonal elements of the focused $\mathbf{R}-$matrix, $\mathbf{R}_{\boldsymbol{\rho}\boldsymbol{\rho}} = [R(\boldsymbol{\rho}_{\mathrm{in}}, \boldsymbol{\rho}_{\mathrm{out}})]$, enable to probe locally the impact of aberrations and

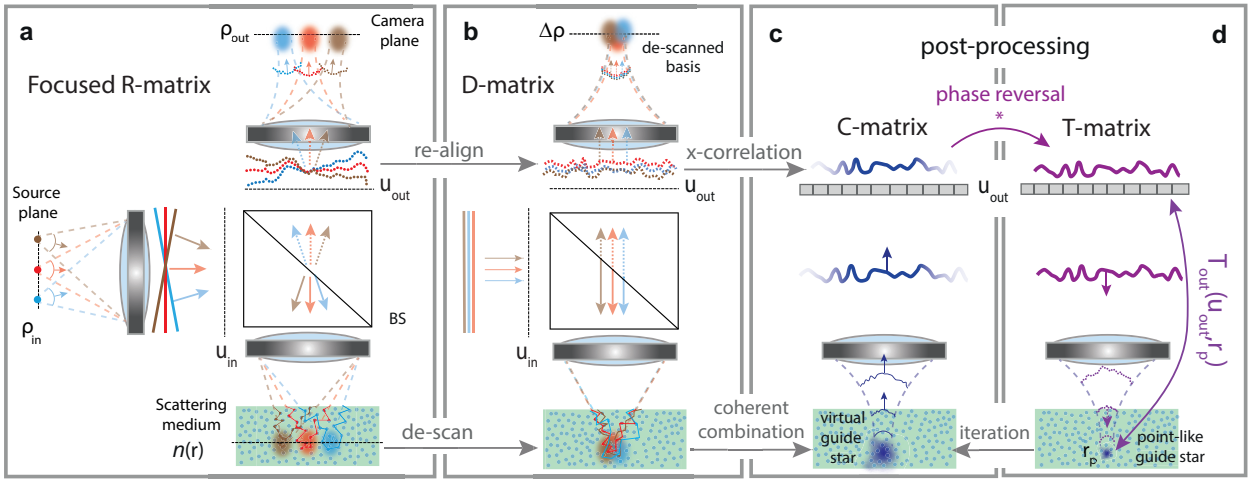

FIG. 1. **Principle of Matrix Imaging. a.** A set of focused wave-fronts is used to illuminate the sample. They can be generated by an array of point-like sources $\boldsymbol{\rho}_{\text{in}}$ conjugated with the focal plane of the microscope objective or by a set of plane waves in the pupil plane ($\mathbf{u}_{\text{in}}$). The reflected wave-fronts are recorded by the pixels $\boldsymbol{\rho}_{\text{out}}$ of a camera also conjugated with the focal plane. The set of impulse responses $R(\boldsymbol{\rho}_{\text{in}}, \boldsymbol{\rho}_{\text{out}})$ between each source $\boldsymbol{\rho}_{\text{in}}$ and detector $\boldsymbol{\rho}_{\text{out}}$ form the focused reflection matrix $\mathbf{R}_{\rho\rho} = [R(\boldsymbol{\rho}_{\text{in}}, \boldsymbol{\rho}_{\text{out}})]$. **b.** The reflected wave-fields can be de-scanned as if they were generated by virtual sources all shifted at the origin thereby forming the de-scanned matrix $\mathbf{D}_{\boldsymbol{\Delta\rho}}$ (Eq. 2). In the output pupil plane ($\mathbf{u}_{\text{out}}$), this operation is equivalent to a realignment of wave-fronts, thereby forming the so-called distortion matrix $\mathbf{D}_{\mathbf{ur}}$. **c.** The correlation matrix $\mathbf{C}_{\text{out}}$ between those wave-fronts mimics the time-reversal operator associated with a virtual guide star that results from a coherent average of all the de-scanned focal spots (see Supplementary Section S4). **d.** An iterative phase reversal algorithm is then applied (see Methods). It first consists in a phase conjugation of the wave-front induced by the virtual guide star. The impinging wave-front compensates for aberrations and scattering inside the medium to produce a sharper guide star. The process is iterated and ultimately provides an estimation of $\mathbf{T}_{\text{out}}(\mathbf{r}_{\text{p}})$, the column of $\mathbf{T}_{\text{out}}$ corresponding to the common mid-point $\mathbf{r}_{\text{p}}$ of the input focal spots considered in panel **a**.

multiple scattering.

In that perspective, a de-scan operation is of particular interest (Fig. 1b). Mathematically, it only consists in the following change of coordinates: $(\boldsymbol{\rho}_{\text{in}}, \boldsymbol{\rho}_{\text{out}}) \rightarrow (\boldsymbol{\rho}_{\text{in}} - \boldsymbol{\rho}_{\text{out}}, \boldsymbol{\rho}_{\text{out}})$. The

interest of a de-scanned reflection matrix $\mathbf{D}$ is twofold. First, it constitutes a flexible starting block for a local compensation of wave distortions through a simple change of basis. Second, the dimension of $\mathbf{D}$ is much smaller than the size of $\mathbf{R}$. In the following, we show how low coherence interferometry enables a compressed measurement of $\mathbf{R}$[31,32].

Compressed Sensing of the Reflection Matrix

Inspired by FFOCT[28], the experimental set up consists in a Linnik interferometer (Fig. 2a). In the first arm, a reference mirror is placed in the focal plane of a microscope objective (MO). The second arm contains the scattering sample to be imaged. In FFOCT, the same broadband incoherent light source is used to illuminate the entire field of the microscope objectives. Because of the broad spectrum of the incident light, interferences occur between the two arms provided that the optical path difference through the interferometer is close to zero. The length of the reference arm determines the slice of the sample (coherence volume) to be imaged and is adjusted in order to match with the focal plane of the MO in the sample arm. The backscattered light from each voxel of the coherence volume can only interfere with the light coming from the conjugated point of a reference mirror. The spatial incoherence of the light source actually acts as a physical confocal pinhole (Fig. 2c). All these interference signals are recorded in parallel by the pixels of the camera in the imaging plane. The FFOCT signal is thus equivalent to a time-gated confocal image of the sample but without any lateral raster scanning[33]. It yields the diagonal coefficients, $R(\boldsymbol{\rho}_{\text{out}}, \boldsymbol{\rho}_{\text{out}}, z)$, of $\mathbf{R}_{\boldsymbol{\rho}\boldsymbol{\rho}}(z)$, where z denotes the depth of the coherence volume. Figures 3b and c show en-face and axial FFOCT images of the opaque cornea at different depths. A dramatic loss in contrast is found beyond the epithelium (z>70 μm, see Fig. 3g). It highlights the detrimental effect of multiple scattering for deep optical imaging.

To overcome the multiple scattering phenomenon, the illumination scheme is slightly modified compared with FFOCT (Fig. 2a). The incident wave-fields are still identical in each arm but are laterally shifted with respect to each other by a transverse position $\Delta\boldsymbol{\rho}$. Their spatial incoherence now acts as a de-scanned pinhole that gives access to the cross-talk between distinct focusing points (Fig. 2b). The interferogram recorded by the camera

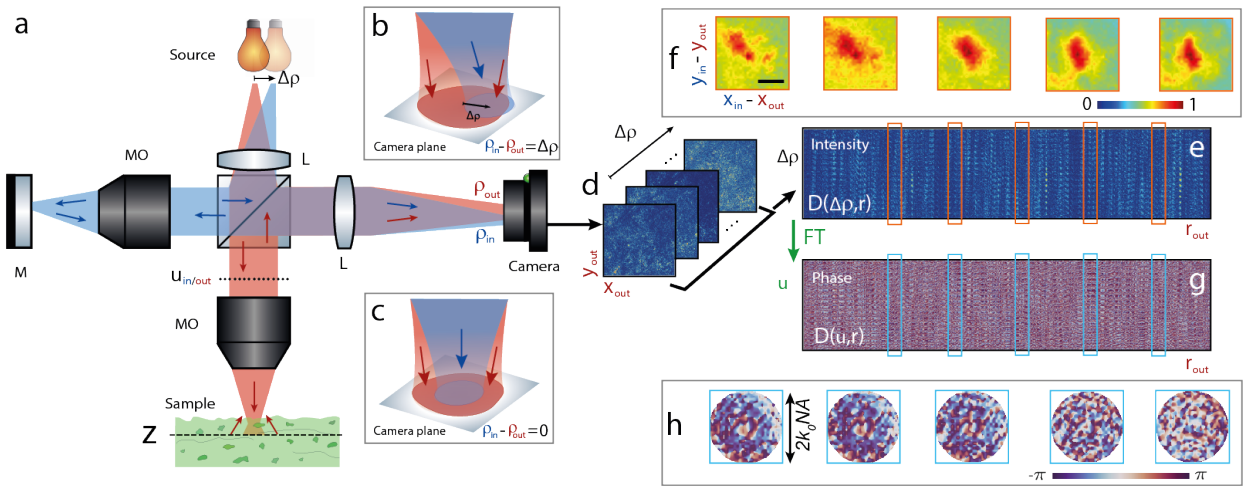

FIG. 2. **Compressed Sensing of the Reflection Matrix. a** Experimental setup (L: lenses, MO: microscope objectives, and M: reference mirror.). Light from an incoherent source is split into two replica laterally shifted with respect to each other by a relative position $\Delta\boldsymbol{\rho}$ (see Supplementary Section S1). By a game of polarization, each replica illuminates one arm of a Linnik interferometer. The sample beam (in red) illuminates the scattering sample through a microscope objective ($NA = 1.0$). The reference beam (in blue) is focused on a dielectric mirror through an identical microscope objective. Both reflected beams interfere on a CMOS camera whose surface is conjugated with focal planes of the MO. The amplitude and phase of the interference term are retrieved by phase-shifting interferometry. **b** Each pixel of the camera, depicted by its position $\boldsymbol{\rho}_{\rm out}$, measures the reflection coefficient $R(\boldsymbol{\rho}_{\rm in}, \boldsymbol{\rho}_{\rm out}, z)$ between de-scanned focusing points, $\mathbf{r}_{\rm out} = (\boldsymbol{\rho}_{\rm out}, z)$ and $\mathbf{r}_{\rm in} = (\boldsymbol{\rho}_{\rm out}+\Delta\boldsymbol{\rho}, z)$, at depth z of the sample. **c** For $\Delta\boldsymbol{\rho} = \mathbf{0}$, the experimental set up is equivalent to a FFOCT apparatus and the interferogram directly provides a time-gated confocal image of the sample. **d** The set of interferograms are stored in the de-scanned reflection matrix $\mathbf{D}_{\Delta\boldsymbol{\rho}}(z) = [D(\Delta\boldsymbol{\rho}, \boldsymbol{\rho}_{\rm out}, z)]$ displayed in panel **e**. **f** Each column of this matrix yields a reflection point-spread function (RPSF) associated with the focusing quality at point $\boldsymbol{\rho}_{\rm out}$ (scale bar: 2 μm). **g** The Fourier transform of each de-scanned wave-field provides the distortion matrix $\mathbf{D}_{\mathbf{ur}}(z) = [D(\mathbf{u}_{\rm in}, \boldsymbol{\rho}_{\rm out}, z)]$. **h** Each column of this matrix displays the distorted wave-front associated with each point $\boldsymbol{\rho}_{\rm out}$ in the field-of-view. The optical data shown in panels d-h correspond to the acquisition performed at depth $z = 150$ μm.

(Fig. 2d) directly provides one line of the de-scanned matrix $\mathbf{D}$, such that

$$D(\Delta\boldsymbol{\rho}, \boldsymbol{\rho}_{\rm out}, z) = R(\boldsymbol{\rho}_{\rm in} + \Delta\boldsymbol{\rho}, \boldsymbol{\rho}_{\rm out}, z). \tag{1}$$

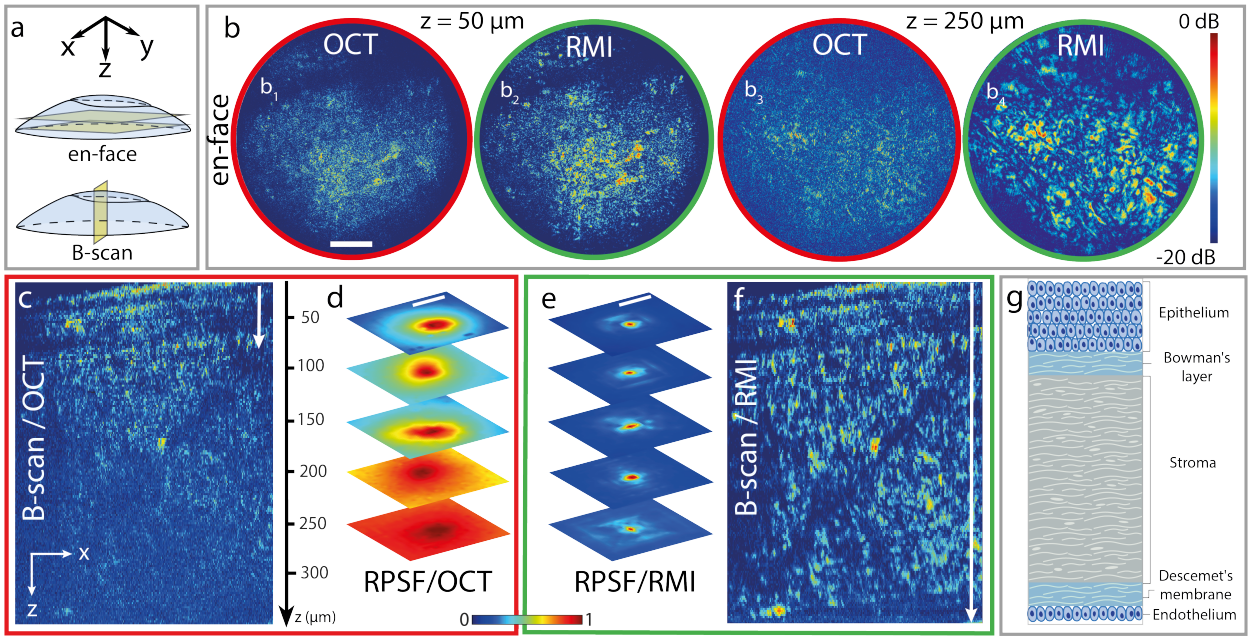

FIG. 3. **Volumetric matrix imaging of an opaque cornea. a.** Schematic of the imaging planes in the cornea. **b.** *En-face* confocal images before ($\mathbf{b}_1$,$\mathbf{b}_3$) and after ($\mathbf{b}_2$,$\mathbf{b}_4$) the matrix imaging process for $z = 50$ μm and 250 μm, respectively (scale bar: 50 μm). **c.** Longitudinal (x,z) section of the initial confocal image. **d.** Original RSPFs from $z = 50$ to 250 μm (scale bar: 1 μm). **e.** Corresponding RPSFs after the matrix imaging process. **f.** Longitudinal (x,z) section of the volumetric image at the end of the matrix imaging process. **g.** Schematic of a healthy human cornea.

Scanning the relative position $\Delta\boldsymbol{\rho}$ is equivalent to recording the $\mathbf{R}$-matrix diagonal-by-diagonal when expressed in a canonical basis (Fig. 1a). However, while a canonical (column-by-column) acquisition of $\mathbf{R}$ requires to illuminate the sample over a field-of-view Ω with $N = (\Omega/\delta_0)^2$ input wave-fronts, the de-scanned basis implies a much smaller number of illuminations.

This sparsity can be understood by expressing theoretically the $\mathbf{D}$-matrix (Supplementary Section S2):

$$D(\Delta\boldsymbol{\rho}, \boldsymbol{\rho}_{\text{out}}, z) = \int_{\Omega} d\boldsymbol{\rho}\, H_{\text{in}}(\boldsymbol{\rho} + \Delta\boldsymbol{\rho}, \mathbf{r}_{\text{in}})\gamma(\boldsymbol{\rho} + \boldsymbol{\rho}_{\text{out}}, z)H_{\text{out}}(\boldsymbol{\rho}, \mathbf{r}_{\text{out}}) \tag{2}$$

where γ is the sample reflectivity. $H_{\text{in}}(\boldsymbol{\rho}, \mathbf{r}_{\text{in}})$ and $H_{\text{out}}(\boldsymbol{\rho}, \mathbf{r}_{\text{out}})$ are the local input and output point spread functions (PSFs) at points $\mathbf{r}_{\text{in}} = (\boldsymbol{\rho}_{\text{in}}, z)$ and $\mathbf{r}_{\text{out}} = (\boldsymbol{\rho}_{\text{out}}, z)$, respectively. This last equation confirms that the central line of $\mathbf{D}_{\Delta\boldsymbol{\rho}}$ ($\Delta\boldsymbol{\rho} = \mathbf{0}$), i.e. the FFOCT image, results from a convolution between the sample reflectivity γ and the local confocal PSF, $H_{\text{in}} \times H_{\text{out}}$.

The de-scanned elements allow us to go far beyond standard imaging. In particular, they

will be exploited to unscramble the local input and output PSFs in the vicinity of each focal point. As a preliminary step, they can also be used to quantify the level of aberrations and multiple scattering. In average, the de-scanned intensity, $I(\Delta\boldsymbol{\rho}, \mathbf{r}_{\rm out}) = |D(\Delta\boldsymbol{\rho}, \boldsymbol{\rho}_{\rm out}, z)|^2$, can actually be expressed as the convolution between the incoherent input and output PSFs[34]:

$$\langle I(\Delta\boldsymbol{\rho}, \mathbf{r}_{\rm out})\rangle \propto |H_{\rm in}|^2 \overset{\Delta\boldsymbol{\rho}}{\circledast} |H_{\rm out}|^2(\Delta\boldsymbol{\rho}, \mathbf{r}_{\rm out}) \tag{3}$$

where the symbol $\circledast$ stands for correlation product and $\langle\cdots\rangle$ for ensemble average. This quantity will be referred to as RPSF in the following (acronym for reflection PSF). Figure 2e displays examples of RSPF extracted in depth of the opaque cornea. Their spatial extension $\delta_{\rm R}$ of the RPSF indicates the focusing quality and dictates the number M of central lines of $\mathbf{D}_{\Delta\boldsymbol{\rho}}(z)$ that contain the relevant information for imaging:

$$M \sim (\delta_R/\delta_0)^2 \tag{4}$$

with $\delta_0 \sim \lambda/(4NA)$, the confocal maximal resolution of the imaging system. For a field-of-view much larger than the spatial extension of the RPSF ($\Omega >> \delta_R$), the de-scanned basis is thus particularly relevant for the acquisition of $\mathbf{R}$ ($M << N$).

Quantifying the Focusing Quality

Figure 3d shows the depth evolution of the RPSF. It exhibits the following characteristic shape: a distorted and enlarged confocal spot on top of an incoherent background[34]. The former component is a manifestation of aberrations; the latter contribution is due to multiple scattering. Figure 3d clearly highlights two regimes. In the epithelium ($z < 70$ μm), the confocal component is predominant and the image of the cornea is reliable although its resolution is affected by aberrations (Fig. 3b$_1$). Beyond this depth, the multiple scattering background is predominant and drastically blurs the image (Fig. 3b$_3$). The axial evolution of the confocal-to-multiple scattering ratio enables the measurement of the scattering mean free path ℓ_s[35] (Supplementary Section S3). We find $\ell_s \sim 70$ μm in the stroma (Fig. 3g), which confirms the strong opacity of the cornea. The penetration depth limit thus scales as ℓ_S. This value is modest compared with theoretical predictions[24] ($\sim 3\ell_S$) but is explained by the occurrence of strong aberrations at shallow depths, partially due to the index mismatch at the cornea surface (Fig. 3d).

The RSPF also fluctuates in the transverse direction. To that aim, a map of local RPSFs (Fig. 4c) can be built by considering the back-scattered intensity over limited spatial windows (Methods). This map shows important fluctuations of aberrations and multiple scattering across the field-of-view due to the lateral variations of the optical index upstream of the focal plane. Such complexity implies that any point in the medium will be associated with its own distinct focusing law. Nevertheless, spatial correlations subsist between RSPFs in adjacent windows (Fig. 4c). Such correlations can be explained by a physical phenomenon often referred to as isoplanatism in adaptive optics[36] and that results in a locally-invariant PSF[37]. We will now see how this local isoplanicity can be exploited for the estimation of the **T**-matrices.

Iterative Phase Reversal of Wave Distortions

Beyond a direct quantification of aberration and scattering problems, the **D**-matrix can be leveraged for their compensation. Indeed, a Fourier transform over the coordinate $\Delta\boldsymbol{\rho}$ of each de-scanned wave-field, $D(\Delta\boldsymbol{\rho}, \mathbf{r}_{\text{out}})$, directly yields the wave distortions seen from the input pupil plane :

$$\mathbf{D_{ur}} = \mathbf{F} \times \mathbf{D_{\Delta r}} \tag{5}$$

where $\mathbf{F}$ denotes the Fourier transform operator, $F(\mathbf{u}, \Delta\boldsymbol{\rho}) = \exp(-i2\pi\mathbf{u}.\Delta\boldsymbol{\rho}/\lambda f)$, λ the central wavelength and f the MO focal length. $\mathbf{D_{ur}} = \mathbf{D_{u\rho}}(z) = [D(\mathbf{u}_{\text{in}}, \boldsymbol{\rho}_{\text{out},}, z)]$ is the distortion matrix that connects any voxel ($\mathbf{r}_{\text{out}}$) in the field-of-view to wave-distortions in the input pupil plane ($\mathbf{u}_{\text{in}}$).

As the RPSF displayed in Fig. 4c, this matrix exhibits local correlations that can be also understood in light of the optical memory effect[38,39]. Waves produced by nearby points inside a complex medium generate highly correlated random speckle patterns in the far field[37,40,41]. Figure 2 illustrates this fact by displaying an example of distortion matrix (Fig. 2g) and reshaped distorted wave-fields for different points $\mathbf{r}_{\text{out}}$ (Fig. 2h). A strong similarity can be observed between distorted wave-fronts associated with neighboring points but this correlation tends to vanish when the two points are too far away.

The next step is to extract and exploit the local memory effect in **D** for imaging. To that aim, a set of correlation matrices $\mathbf{C}_{\text{in}}(\mathbf{r}_{\text{p}})$ shall be considered between distorted wave-fronts in the vicinity of each point $\mathbf{r}_{\text{p}}$ in the field-of-view (Methods). Under the hypothesis of

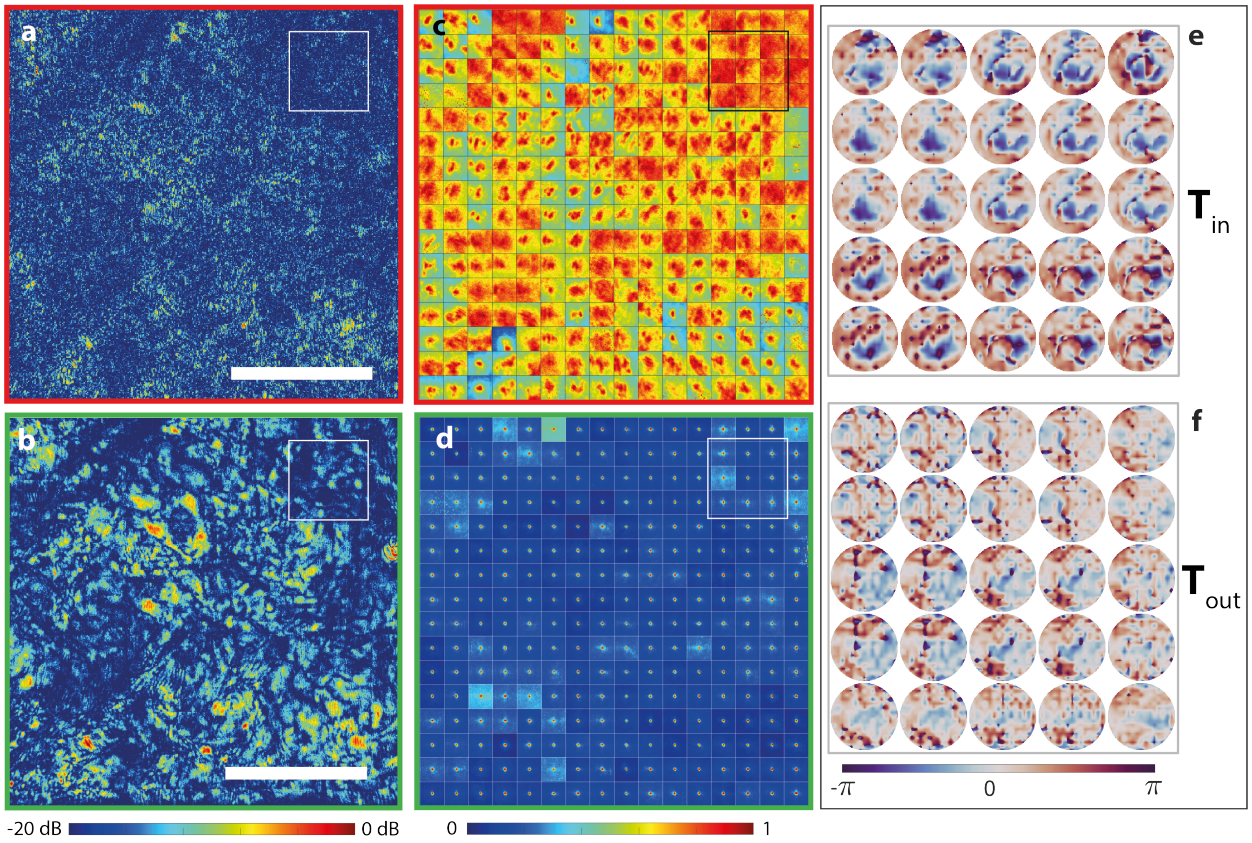

FIG. 4. **Inner Transmission matrix for Local Compensation of Forward Multiple Scattering. a,b.** Confocal field of view before and after the correction process at 200 μm-depth, respectively (scale bar: 50 μm). **c,d.** Maps of the local reflection point-spread functions (RPSFs) (de-scan field-of-view: 7×7 μm^2) over the field of view, before and after the correction process, respectively. **e,f.** Sub-part of matrices, $\hat{\mathbf{T}}_{\text{in}}$ and $\hat{\mathbf{T}}_{\text{out}}$, respectively, for the area delimited by the square box in panels **a**-**d**.

local isoplanicity, each matrix $\mathbf{C}_{\text{in}}(\mathbf{r}_{\text{p}})$ is analogous to a $\mathbf{R}$-matrix associated with a virtual reflector synthesized from the set of output focal spots[21] (see Fig. 1c and Supplementary Section S4). In this fictitious experimental configuration, an iterative phase-reversal process can be performed to converge towards the incident wave front that focuses perfectly through the heterogeneities of the medium onto this virtual scatterer (see Fig. 1d and Methods).

This iterative phase reversal algorithm, repeated for each point $\mathbf{r}_{\text{p}}$, yields an estimator $\hat{\mathbf{T}}_{\text{in}}$ of the transmission matrix, $\mathbf{T}_{\text{in}} = \mathbf{F} \times \mathbf{H}_{\text{in}}$. Its digital phase conjugation enables a local compensation of aberration and multiple scattering. An updated de-scanned matrix can then

be built:

$$\mathbf{D}_{\Delta\mathbf{r}} = \mathbf{F}^{\dagger} \times \left[\hat{\mathbf{T}}_{\text{in}}^{*} \circ \mathbf{D}_{u\mathbf{r}} \right] \tag{6}$$

where the symbol † stands for transpose conjugate and ∘ for the Hadamard product. The same process can be repeated by exchanging input and output to estimate the output transmission matrix $\mathbf{T}_{\text{out}}$ (Methods).

Multi-Scale analysis of the Distortion Matrix

A critical aspect of RMI is the choice of the spatial window over which wave distortions shall be analyzed. On the one hand, the isoplanatic assumption is valid for low-order aberrations that are associated with extended isoplanatic patches. Forward multiple scattering, on the other hand, gives rise to high-order aberration that exhibits a coherence length that decreases with depth until reaching the size of a speckle grain beyond ℓ_t[37]. However, the spatial windows should be large enough to encompass a sufficient number of independent realizations of disorder[42]. Indeed, this number should be one order of magnitude larger than the size M of the aberrated focal spot in terms of resolution cells. If the latter condition is not fulfilled, the iterative phase reversal process indeed cannot converge towards a correct estimator (Supplementary Section S5).

To satisfy these two contradictory conditions, an iterative multi-scale strategy is proposed for the analysis of the $\mathbf{D}-$matrix. It consists in iterating the RMI process while dividing by two the size of overlapping spatial windows at each iterative step (Fig. a). At each iteration, the RPSF extension decreases (Fig. b) and the spatial window can be reduced accordingly at the next step. It enables the capture of finer angular and spatial details of the $\mathbf{T}-$matrix at each step (Fig. c) while ensuring the convergence of the iterative phase reversal algorithm. At the end of the process (Supplementary Section S5), each individual patch covers an area of 6×6 μm^2 which provides the spatial resolution of the $\mathbf{T}-$matrix estimator.

Transmission Matrix and Memory Effect

Figures 4e and f show a sub-part of the $\mathbf{T}$-matrices measured at depth $z = 200$ μm. Spatial reciprocity should imply equivalent input and output aberration phase laws. This property is not checked by our estimators. Indeed, the input aberration phase law accumulates not only

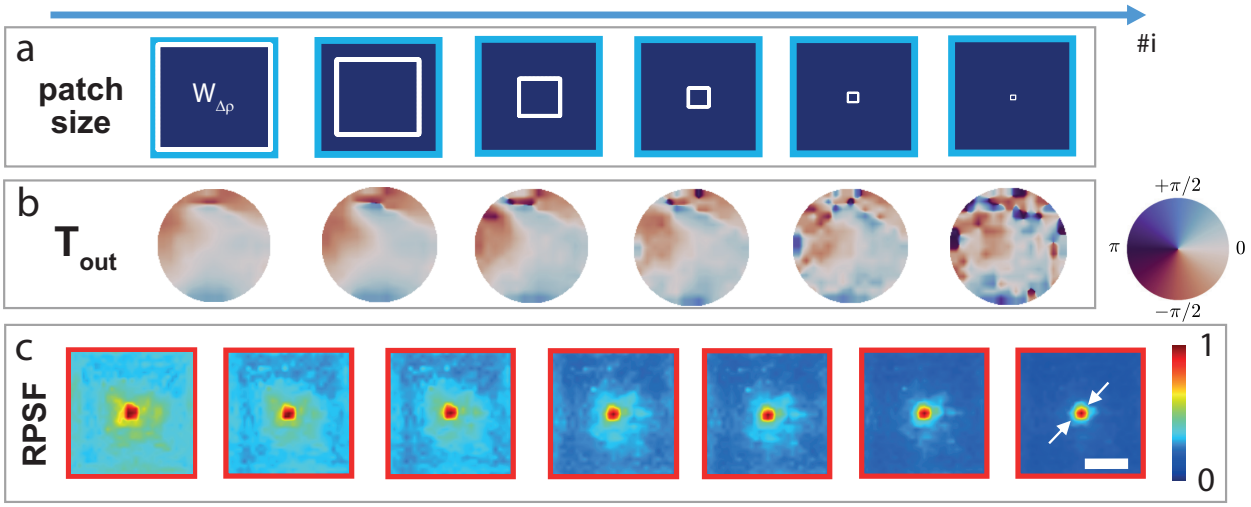

FIG. 5. **Multi-scale analysis of wave distortions. a.** The entire field-of-view is $138 \times 138 \mu m^2$. At each step, it is divided into a set of spatial windows whose dimension gradually decreases: from 138, 100, 50, 25, 13 to 6 μm **b.** Evolution of the transmitted wave-front $\hat{T}(\mathbf{u}_{\text{out}}, \mathbf{r}_p)$ for one point $\mathbf{r}_\text{p}$ of the field-of-view at each iteration step. **c.** Corresponding local RPSF at $\mathbf{r}_\text{p}$ before and after compensation of aberration and scattering using digital phase-conjugation of the optical transfer function displayed in panel **b** (scale bar: 2 μm). Data are from the cross-section at 200μm depth within the sample.

the input aberrations of the sample-arm but also those of the reference arm (Supplementary Section S2). Therefore, the sample-induced aberrations can be investigated independently from the imperfections of the experimental set up by considering the output matrix $\hat{\mathbf{T}}_{\text{out}}$.

An analysis of its spatial correlations clearly shows that wave distortions induced by the cornea are made of two contributions (Methods):(i) a spatially-invariant aberrated component (Fig. 6a) associated with long-scale fluctuations of the refractive index (Fig. 6c) ; (ii) a forward multiple scattering component (Fig. 6d) associated with isoplanatic patches whose size drastically decreases in depth (Fig. 6a,e).

Deep Volumetric Imaging

Eventually, the estimated **T**-matrices can be used to compensate for local aberrations over the whole field-of-view, by digital phase conjugation performed at input and output (Eq. 6). The comparison between the initial and resulting images (Figs. 4a,b) demonstrates the benefit

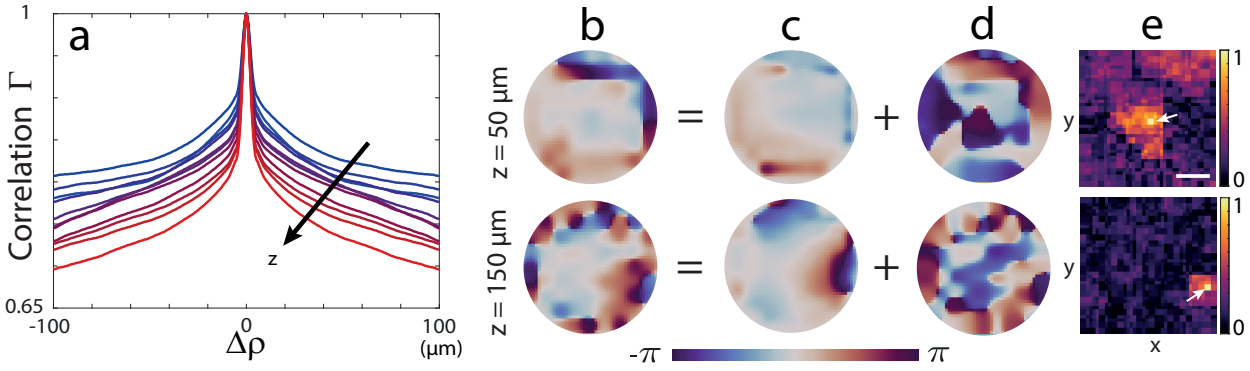

FIG. 6. Revealing the memory effect exhibited by the **T**−matrix. **a.** Transverse evolution of the mean correlation function of the transmitted wave-field from shallow (blue) to large (red) depths. **b.** The phase of each transmitted wave-field is the sum of: **c.** a spatially-invariant aberration phase function; **d.** a complex scattering law exhibiting high spatial frequencies. **e.** The spatial correlation of the latter component with the **T**−matrix provides a map of the corresponding isoplanatic patch (scale bar: 50μm).

of a local compensation of aberration and scattering. The drastic gain in resolution and contrast provided by RMI enables to reveal a rich arrangement of biological structures (cells, striae, *etc.*) that were completely blurred by scattering in the initial image. For instance, a stromal stria, indicator of keratoconus[43], is clearly revealed on the RMI B-scan (Fig. 3f) while it was hidden by the multiple scattering fog on the initial image (Fig. 3c). The B-scan shows that RMI provides a full image of the cornea with the recovery of its different layers throughout its thickness (350 μm $\sim 5\ell_s$, see also Supplementary Movies).

The gain in contrast and resolution can be quantified by investigating the RSPF after RMI. A close-to-ideal confocal resolution (230 nm vs. $\delta_0 \sim 215$ nm) is reached throughout the cornea thickness (Fig. 3e). The confocal-to-diffuse ratio is increased by a factor up to 15 dB in depth (Supplementary Section S6). Furthermore, the map of local RPSFs displayed in Fig. 4d shows the efficiency of RMI for addressing extremely small isoplanatic patches.

Discussion

Although this experimental proof-of-concept is spectacular and promising for deep optical imaging of biological tissues, it suffers from several limitations that need to be addressed in

future works. First, FFOCT is not very convenient for 3D in-vivo imaging since it requires an axial scan of the sample. Another possibility would be to move the reference arm and measure $\mathbf{R}$ as a function of the time-of-flight.

An access to the time (or spectral) dependence of the $\mathbf{R}-$matrix is actually critical to reach a penetration depth larger than ℓ_t. Indeed, the aberration phase law extracted from a time-gated $\mathbf{R}$-matrix is equivalent in the time domain to a simple application of time delays between each angular component of the wave-field. Yet, the diffusive regime requires to address independently each frequency component of the wave-field to make multiple scattering paths of different lengths constructively interfere on any focusing point in depth.

Beyond the diffusive regime, another blind spot of this study is the medium movement during the experiment[44,45]. In that respect, the matrix formalism shall be developed to include the medium dynamics. Moving speckle can actually be an opportunity since it can give access to a large number of speckle realizations for each voxel. A high resolution $\mathbf{T}-$matrix could be, in principle, extracted without relying on any isoplanatic assumption[46].

To conclude, this study is a striking illustration of a pluri-disciplinary approach in wave physics. A passive measurement of the $\mathbf{R}$-matrix is indeed an original idea coming from seismology[47]. The $\mathbf{D}$-matrix is inspired by stellar speckle interferometry in astronomy[48]. The $\mathbf{T}$-matrix is a concept that has emerged both from fundamental studies in condensed matter physics[8] and more applied fields such as MIMO communications[10] and ultrasound therapy[12]. The emergence of high-speed cameras and the rapid growth of computational capabilities now makes matrix imaging mature for deep in-vivo optical microscopy.

Methods

Experimental set up

The full experimental setup is displayed in Supplementary Figure S1. It is made of two parts: (i) a polarized Michelson interferometer illuminated by a broadband LED source (Thorlabs M850LP1, $\lambda_\circ = 850$ nm, $\Delta\lambda = 35$ nm) in a pseudo-Kohler configuration, thereby providing at its output two identical spatially-incoherent and broadband wave-fields of orthogonal polarization, the reference one being shifted by a lateral position $\Delta\boldsymbol{\rho}$ by tilting the mirror in the corresponding arm; (ii) a polarized Linnik interferometer with microscope objectives (Nikon N60X-NIR, $M = 60\times$, $NA = 1.0$) in the two arms and a CMOS camera (Adimec Quartz 2A-750, 2Mpx) at its output. The de-scanned beam at the output the first interferometer illuminates the reference arm of the second interferometer and is reflected by the reference mirror placed in the focal plane of the MO. The other beam at the output of the first interferometer illuminates the sample placed in the focal plane of the other MO. The CMOS camera, conjugated with the focal planes of the MO, records the interferogram between the beams reflected by each arm of the Linnik interferometer. The spatial sampling of each recorded image is $\delta_0 = 230$ nm and the field-of-view is 275×275 μm^2

Experimental procedure

The experiment consists in the acquisition of the de-scanned reflection matrix $\mathbf{D}_{\Delta\mathbf{r}}$. To that aim, an axial scan of the sample is performed over the cornea thickness (350 μm) with a sampling of 2 μm (i.e 185 axial positions). For each depth, a transverse scan of the de-scanned position $\Delta\boldsymbol{\rho}$ is performed over a 2.9×2.9 μm^2 area with a spatial sampling $\delta_0 = 230$ nm (that is to say 169 input wave-fronts instead of 10^6 input wave-fronts in a canonical basis). For each scan position $(\Delta\rho, z)$, a complex-reflected wave field is extracted by phase shifting interferometry from four intensity measurements. This measured field is averaged over 5 successive realisations (for denoising). The integration time of the camera is set to 5 ms. Each wave-field is stored in the de-scanned reflection matrix $\mathbf{D}_{\Delta\mathbf{r}} = [D(\Delta\boldsymbol{\rho}, \boldsymbol{\rho}_{\text{out}})]$ (Fig. 2). The duration time for the recording of $\mathbf{D}_{\Delta\boldsymbol{\rho}}$ is of ~ 30 s at each depth. The post-processing of the reflection matrix (iterative phase reversal and multi-scale analysis) to get the final image took only a few minutes on Matlab. The experimental results displayed in Fig. 4 and at a single depth $z = 200$ μm have been obtained by performing a de-scan over a 7×7 μm^2 area with a spatial sampling $\delta_0 = 230$ nm (961 input wave-fronts).

Local RPSF

To probe the local RPSF, the field-of-view is divided into regions that are defined by their central midpoint $\mathbf{r}_\mathrm{p}$ and their spatial extension L. A local average of the back-scattered intensity can then be performed in each region:

$$I(\Delta\boldsymbol{\rho}, \mathbf{r}_p) = \langle |D(\Delta\boldsymbol{\rho}, \mathbf{r}_\mathrm{out})|^2 W_L(\mathbf{r}_\mathrm{out} - \mathbf{r}_p)\rangle_{\mathbf{r}_\mathrm{out}} \tag{7}$$

where $W_L(\mathbf{r}_\mathrm{out} - \mathbf{r}_p) = 1$ for $|\boldsymbol{\rho}_\mathrm{out} - \boldsymbol{\rho}_p| < L$, and zero otherwise.

Local correlation matrix

A set of correlation matrices shall be considered between distorted wave-fronts associated with different regions of the field-of-view:

$$C_\mathrm{in}(\mathbf{u}_\mathrm{in}, \mathbf{u}'_\mathrm{in}, \mathbf{r}_p) = \langle D(\mathbf{u}_\mathrm{in}, \mathbf{r}_\mathrm{out}) D^*(\mathbf{u}'_\mathrm{in}, \mathbf{r}_\mathrm{out}) W_L(\mathbf{r}_\mathrm{p} - \mathbf{r}_\mathrm{out})\rangle_{\mathbf{r}_\mathrm{out}} \tag{8}$$

Iterative phase reversal algorithm.

The iterative phase reversal algorithm is a computational process that provides an estimator of the transmit wave-field $T(\mathbf{u}, \mathbf{r}_p)$ that links each point $\mathbf{u}$ of the pupil plane with each voxel $\mathbf{r}_\mathrm{p}$ of the cornea volume. To that aim, the correlation matrix $\mathbf{C}$ computed over the spatial window W_L centered around each point $\mathbf{r}_\mathrm{p}$ is considered (Eq. 8). Mathematically, the algorithm is based on the following recursive relation:

$$\hat{\mathbf{T}}^{(n)}(\mathbf{r}_p) = \exp\left[i \arg\left\{\mathbf{C}(\mathbf{r}_p) \times \hat{\mathbf{T}}^{(n-1)}(\mathbf{r}_p)\right\}\right] \tag{9}$$

where $\hat{\mathbf{T}}^{(n)}$ is the estimator of $\mathbf{T}$ at the n^th iteration of the phase reversal process. $\hat{\mathbf{T}}^{(0)}$ is an arbitrary wave-front that initiates the iterative phase reversal process (typically a flat phase law) and $\hat{\mathbf{T}} = \lim_{n\to\infty} \hat{\mathbf{T}}^{(n)}$ is the result of this iterative phase reversal process.

Aberration and Scattering compensation at output.

The output de-scanned matrix $\mathbf{D}_{\Delta\boldsymbol{\rho}}(z)$ is deduced from the input de-scanned matrix $\mathbf{D}_{\Delta\boldsymbol{\rho}}(z)$ using the following change of variable:

$$D(\boldsymbol{\rho}_\mathrm{in}, \Delta\boldsymbol{\rho}', z) = D(-\Delta\boldsymbol{\rho}', \boldsymbol{\rho}_\mathrm{in} + \Delta\boldsymbol{\rho}', z) \tag{10}$$

with $\Delta\boldsymbol{\rho}' = \boldsymbol{\rho}_\mathrm{out} - \boldsymbol{\rho}_\mathrm{in} = -\Delta\boldsymbol{\rho}$.

An output distortion matrix is then built by applying a Fourier transform over the de-scanned coordinate:

$$\mathbf{D_{ru}} = \mathbf{D_{\Delta r}} \times \mathbf{F}^T \tag{11}$$

where the superscript ^{T} stands for matrix transpose. From $\mathbf{D_{ru}}$, one can build a correlation matrix $\mathbf{C}_{\rm out}$ for each point $\mathbf{r}_{\rm p}$:

$$C_{\rm out}(\mathbf{u}_{\rm out}, \mathbf{u}'_{\rm out}, \mathbf{r}_p) = \langle D(\mathbf{r}_{\rm in}, \mathbf{u}_{\rm out}) D^*(\mathbf{r}_{\rm in}, \mathbf{u}'_{\rm out}) W_L(\mathbf{r}_{\rm p} - \mathbf{r}_{\rm out}) \rangle_{\mathbf{r}_{\rm out}} \tag{12}$$

The iterative phase reversal algorithm described above is then applied to each matrix $\mathbf{C}_{\rm out}(\mathbf{r}_p)$ to derive an estimator $\hat{\mathbf{T}}_{\rm out}$ of the output $\mathbf{T}$-matrix.

Aberration and Scattering Components of the T-matrix.

The spatial correlation of transmitted wave-fields are investigated at each depth z by computing the correlation matrix of $\mathbf{T}_{\rm out}$: $\mathbf{C_T} = \mathbf{T}_{\rm out} \times \mathbf{T}^\dagger_{\rm out}$. A mean correlation function Γ can be computed by performing the following average:

$$\Gamma(\Delta\boldsymbol{\rho}, z) = \langle C_T(\boldsymbol{\rho}_{\rm in}, \boldsymbol{\rho}_{\rm in} + \Delta\boldsymbol{\rho}, z) \rangle_{\boldsymbol{\rho}_{\rm in}} \tag{13}$$

The correlation function Γ displayed in Fig. 6a shows that the matrix $\mathbf{T}_{\rm out}$ can be decomposed as a spatially-invariant component $\mathbf{T}^{(a)}_{\rm out}$ and a short-range correlated component $\mathbf{T}^{(m)}_{\rm out}$. Each component can be separated by performing a singular value decomposition of $\mathbf{T}_{\rm out}$, such that

$$\mathbf{T}_{\rm out} = \sum_{p=1}^{N} s_p \mathbf{U}_p \mathbf{V}_p^\dagger \tag{14}$$

where s_p are the positive and real singular values of $\mathbf{T}_{\rm out}$ ranged in decreasing order, $\mathbf{U}_p$ and $\mathbf{V}_p$ are unitary matrices whose columns correspond to the input and output singular vectors of $\mathbf{T}_{\rm out}$. The first eigenspace of $\mathbf{T}_{\rm out}$ provides its spatially-invariant component: $\mathbf{T}^{\rm (a)}_{\rm out} = s_1 \mathbf{U}_1 \mathbf{V}_1^\dagger$. The higher rank eigenstates provide the multiple scattering component $\mathbf{T}^{(m)}_{\rm out}$. Lines or columns of the associated correlation matrix $\mathbf{C}^{(m)}_T = \mathbf{T}^{(m)}_{\rm out} \times \mathbf{T}^{(m)\dagger}_{\rm out}$ provides the map of isoplanatic patches displayed in Fig. 6e.

Acknowledgments. The authors wish to thank A. Badon for initial discussions about the experimental set up, K. Irsch for providing the corneal sample and A. Le Ber for providing the iterative phase reversal algorithm.

Funding Information. The authors are grateful for the funding provided by the European Research Council (ERC) under the European Union's Horizon 2020 research and innovation program (grant agreement nos. 610110 and 819261, HELMHOLTZ* and REMINISCENCE projects, respectively). This project has also received funding from Labex WIFI (Laboratory of Excellence within the French Program Investments for the Future; ANR-10-LABX-24 and ANR-10-IDEX-0001-02 PSL*).

Author Contributions. A.A. initiated and supervised the project. A.C.B., V.B. and A.A. designed the experimental setup. U.N., V.B. and P.B. built the experimental set up. U.N. and V.B. developed the post-processing tools. U.N. performed the corneal imaging experiment. U.N. and A.A. analyzed the experimental results. V.B.and A.A. performed the theoretical study. A.A. and U.N. prepared the manuscript. U.N., V.B., P.B., M.F., A.C.B., and A.A. discussed the results and contributed to finalizing the manuscript.

Competing interests. A.A., M.F., A.C.B. and V.B. are inventors on a patent related to this work held by CNRS (no. US11408723B2, published August 2022). All authors declare that they have no other competing interests.

[1] B. Gérardin, J. Laurent, A. Derode, C. Prada, and A. Aubry, Phys. Rev. Lett. **113**, 173901 (2014).

[2] M. Horodynski, M. Kühmayer, C. Ferise, S. Rotter, and M. Davy, Nature **607**, 281 (2022).

[3] J. Billy, V. Josse, Z. Zuo, A. Bernard, B. Hambrecht, P. Lugan, D. Clément, L. Sanchez-Palencia, P. Bouyer, and A. Aspect, Nature **453**, 891 (2008).

[4] H. Hu, A. Strybulevych, J. H. Page, S. E. Skipetrov, and B. A. van Tiggelen, Nat. Phys. **4**, 945 (2008).

[5] V. Ntziachristos, Nat. Methods **7**, 603 (2010).

[6] J. Bertolotti and O. Katz, Nat. Phys. **18**, 1008 (2022).

[7] A. P. Mosk, A. Lagendijk, G. Lerosey, and M. Fink, Nat. Photonics **6**, 283 (2012).

[8] S. Rotter and S. Gigan, Rev. Mod. Phys. **89**, 015005 (2017).

[9] H. Cao, A. P. Mosk, and S. Rotter, Nat. Phys. **18**, 994 (2022).

[10] G. Foschini and M. Gans, Wireless Personal Communications **6**, 311 (1998).

[11] A. Aubry and A. Derode, Phys. Rev. Lett. **102**, 084301 (2009).

[12] M. Tanter, J.-F. Aubry, J. Gerber, J.-L. Thomas, and M. Fink, J. Acoust. Soc. Am. **110**, 37 (2001).

[13] A. Derode, A. Tourin, J. de Rosny, M. Tanter, S. Yon, and M. Fink, Phys. Rev. Lett. **90**, 014301 (2003).

[14] S. M. Popoff, G. Lerosey, R. Carminati, M. Fink, A. C. Boccara, and S. Gigan, Phys. Rev. Lett. **104**, 100601 (2010).

[15] C. W. Hsu, S. F. Liew, A. Goetschy, H. Cao, and A. D. Stone, Nat. Phys. **13**, 497 (2017).

[16] D. Bouchet, S. Rotter, and A. P. Mosk, Nat. Phys. **17**, 564 (2021).

[17] N. Bender, A. Yamilov, A. Goetschy, H. Yılmaz, C. W. Hsu, and H. Cao, Nat. Phys. **18**, 309 (2022).

[18] S. Yoon, M. Kim, M. Jang, Y. Choi, W. Choi, S. Kang, and W. Choi, Nat. Rev. Phys. **2**, 141 (2020).

[19] A. Badon, V. Barolle, K. Irsch, A. C. Boccara, M. Fink, and A. Aubry, Sci. Adv. **6**, eaay7170 (2020).

[20] S. Yoon, H. Lee, J. H. Hong, Y.-S. Lim, and W. Choi, Nat. Commun. **11**, 5721 (2020).

[21] W. Lambert, L. A. Cobus, T. Frappart, M. Fink, and A. Aubry, Proc. Natl. Acad. Sci. U. S. A. **117**, 14645 (2020).

[22] S. Gigan and *et al.*, J. Phys. Photon. **4**, 042501 (2022), chapter 10.

[23] Y. Kwon, J. H. Hong, S. Kang, H. Lee, Y. Jo, K. H. Kim, S. Yoon, and W. Choi, Nat. Commun. **14**, 105 (2023).

[24] A. Badon, A. C. Boccara, G. Lerosey, M. Fink, and A. Aubry, Opt. Express **25**, 28914 (2017).

[25] M. Kim, Y. Jo, J. H. Hong, S. Kim, S. Yoon, K.-D. Song, S. Kang, B. Lee, G. H. Kim, H.-C. Park, and W. Choi, Nat. Commun. **10**, 1 (2019).

[26] S. Kang, S. Jeong, W. Choi, H. Ko, T. D. Yang, J. H. Joo, J.-S. Lee, Y.-S. Lim, Q.-H. Park, and W. Choi, Nat. Photonics **9**, 253 (2015).

[27] A. Badon, D. Li, G. Lerosey, A. C. Boccara, M. Fink, and A. Aubry, Sci. Adv. **2**, e1600370 (2016).

[28] E. Beaurepaire, A. C. Boccara, M. Lebec, L. Blanchot, and H. Saint-Jalmes, Opt. Lett. **23**, 244 (1998).

[29] A. Dubois, L. Vabre, A.-C. Boccara, and E. Beaurepaire, Appl. Opt. **41**, 805 (2002).

[30] S. Kang, P. Kang, S. Jeong, Y. Kwon, T. D. Yang, J. H. Hong, M. Kim, K. Song, J. H. Park, J. H. Lee, M. J. Kim, K. H. Kim, and W. Choi, Nat. Commun. **8**, 2157 (2017).

[31] A. Badon, G. Lerosey, A. C. Boccara, M. Fink, and A. Aubry, Phys. Rev. Lett. **114**, 023901 (2015).

[32] A. Badon, D. Li, G. Lerosey, A. Claude Boccara, M. Fink, and A. Aubry, Optica **3**, 1160 (2016).

[33] V. Barolle, J. Scholler, P. Mecê, J.-M. Chassot, K. Groux, M. Fink, A. C. Boccara, and A. Aubry, Opt. Express **29**, 22044 (2021).

[34] W. Lambert, L. A. Cobus, M. Couade, M. Fink, and A. Aubry, Phys. Rev. X **10**, 021048 (2020).

[35] C. Brütt, A. Aubry, B. Gérardin, A. Derode, and C. Prada, Phys. Rev. E **106**, 025001 (2022).

[36] F. Roddier, ed., *Adaptive Optics in Astronomy* (Cambridge University Press, Cambridge, 1999).

[37] B. Judkewitz, R. Horstmeyer, I. M. Vellekoop, I. N. Papadopoulos, and C. Yang, Nat. Phys. **11**, 684 (2015).

[38] J. Bertolotti, E. G. van Putten, C. Blum, A. Lagendijk, W. L. Vos, and A. P. Mosk, Nature **491**, 232 (2012).

[39] O. Katz, P. Heidmann, M. Fink, and S. Gigan, Nat. Photonics **8**, 784 (2014).

[40] G. Osnabrugge, R. Horstmeyer, I. N. Papadopoulos, B. Judkewitz, and I. M. Vellekoop, Optica **4**, 886 (2017).

[41] L. Zhu, J. B. de Monvel, P. Berto, S. Brasselet, S. Gigan, and M. Guillon, Optica **7**, 338 (2020).

[42] W. Lambert, L. A. Cobus, J. Robin, M. Fink, and A. Aubry, IEEE Trans. Med. Imag. **41**, 3921 (2022).

[43] K. Grieve, D. Ghoubay, C. Georgeon, G. Latour, A. Nahas, K. Plamann, C. Crotti, R. Bocheux, M. Borderie, T.-M. Nguyen, F. Andreiuolo, M.-C. Schanne-Klein, and V. Borderie, Sci. Rep. **7**, 13584 (2017).

[44] M. Jang, H. Ruan, I. M. Vellekoop, B. Judkewitz, E. Chung, and C. Yang, Biomed. Opt. Express **6**, 72 (2014).

[45] J. Scholler, K. Groux, O. Goureau, J.-A. Sahel, M. Fink, S. Reichman, C. Boccara, and K. Grieve, Light Sci. Appl. **9**, 140 (2020).

[46] B.-F. Osmanski, G. Montaldo, M. Tanter, and M. Fink, IEEE Trans. Ultrason. Ferroelectr. Freq. Control **59**, 1575 (2012).

[47] M. Campillo and A. Paul, Science **299**, 547 (2003).

[48] A. Labeyrie, Astron. Astrophys. **6**, 85 (1970).

Supplementary Information for Non-invasive Retrieval of the Transmission Matrix for Optical Imaging Deep Inside a Multiple Scattering Medium

Ulysse Najar, Victor Barolle, Paul Balondrade,
Mathias Fink, A. Claude Boccara, and Alexandre Aubry
Institut Langevin, ESPCI Paris, PSL University, CNRS, Paris, France

Abstract

This document provides further information on: (i) the experimental set up; (ii) the theoretical expression of the de-scanned matrix; (iii) the measurement of the scattering mean free path; (iv) the theoretical expression of the correlation matrix; (v) the estimation of the transmission matrix; (vi) the contrast enhancement provided by reflection matrix imaging.

S1. DETAILED EXPERIMENTAL SET-UP

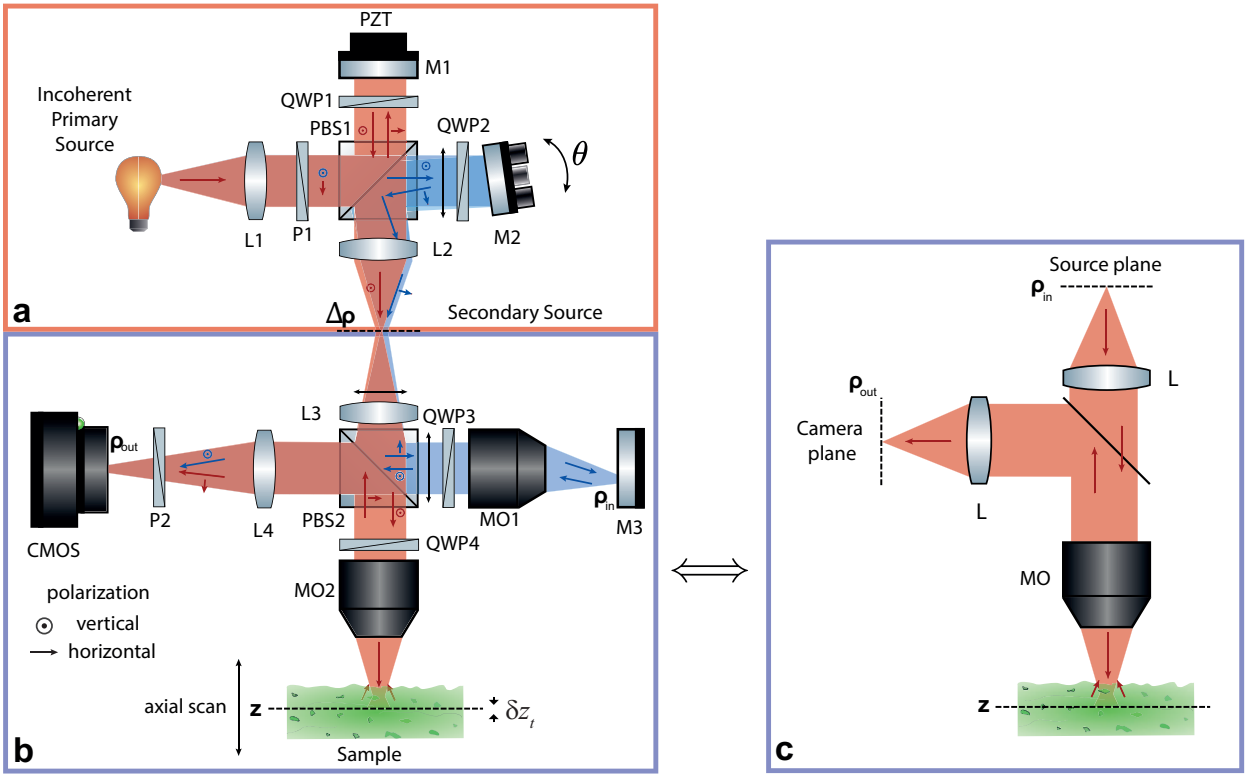

FIG. S1. **Passive measurement of the de-scanned reflection matrix.** P: polarizer, L: lens, QWP: quarter-wave plate, M: mirror, PZT: piezo-electric actuator, PBS: polarisation beam splitter, MO: microscope objective. The apparatus is made up of two parts. **a**. Michelson interferometer illuminated by incoherent light source at its input and generating two twin incoherent beams of orthogonal polarization and laterally shifted from each other at its output. The polarised beam splitters (PBS1) separates the impinging light into a reference path (in blue) and a sample path (in red). The tilt $\delta\theta$ of mirror M2 controls the shift $\Delta\boldsymbol{\rho}$ between the twin beams in the secondary source plane. **b**. Michelson interferometer with microscope objectives (MO) in both arms (Linnik configuration). Both beams have orthogonal polarizations and each interferometer arm includes a quarter-wave plate (QWP). The output beams are collected by the L4 lens and interfere on the camera after having been projected on a 45°-rotated polarizer (P2). **c.** Equivalent layout in the case of a coherent measurement. The source plane, the focal plane, and the camera planes are conjugated. Displacing a point source $\boldsymbol{\rho}_{\text{in}}$ in the source plane discretely scans the focal plane inside the sample. The illuminated area is imaged in the camera plane; in an epi-detection configuration.

The full experimental set up is displayed in Fig. S1. The setup is divided into two building blocks, labelled (a) and (b). The first component is a Michelson interferometer [Fig. S1a]. The light source is a broadband LED (Thorlabs M850LP1, $\lambda_\circ = 850$ nm, $\Delta\lambda = 35$ nm), which, under a pseudo-Kohler configuration, ensures a spatially-incoherent, yet uniform, illumination of the field-of-view. The incident light is collimated using a convergent lens (L1) with a focal length $f_1 = 150$ mm. The beam transmitted through this lens (L1) is linearly polarized at 45° by a polarizer (P1) so that it is then equally reflected (sample arm) and transmitted (reference arm) by the polarized beam splitter (PBS1).

The sample beam reflected by PBS1 is horizontally polarized. It propagates through a quarter-wave plate (QWP1), is reflected by a plane mirror (M1), whose normal lies along the optical axis and that is mounted on a piezoelectric actuator (PZT). The reflected beam passes again through the quarter-wave plate (QWP1). This sequence induces a polarization rotation by 90° of the reflected beam with respect to the incident beam in the sample arm. The reflected wave can be then transmitted through the beam splitter (PBS1) with a vertical polarization and finally focused in a secondary source plane conjugated with the source plane by means of the lens (L2) of focal length $f_2 = 125$ mm.

The reference beam, vertically polarized at the exit of the polarizer (P1), is transmitted by the beam splitter (PBS1), propagates through a quarter-wave plate (QWP2), is reflected by a set of galvanometric scan mirrors (M2) that enables a 2D rotation of the incident wave-field by angles $\boldsymbol{\theta} = (\theta_x, \theta_y)$ with respect to the optical axis. The reflected beam then propagates again through the quarter wave plate (QWP2). This round trip through (QWP2) enables a 90° rotation of the light polarization. The reflected beam is therefore reflected by the beam splitter (PBS1) before being focused by the lens (L2) in the secondary source plane.

Finally, in the secondary source plane, the wave-field is made of two images of the incident light orthogonally polarized and translated with respect each other by a relative position $\Delta\boldsymbol{\rho}$. This lateral shift is dictated by the tilt $\boldsymbol{\theta} = (\theta_x, \theta_y)$ of the reference beam: $\Delta x = f_2 \tan\theta_x$ and $\Delta y = f_2 \tan\theta_y$. Note also that the optical path difference between the two arms is set to zero by equalizing the length of sample and reference arms for $\Delta\boldsymbol{\theta} = 0$.

After the Michelson interferometer, these two orthogonally polarized beams enter a Michelson interferometer with two identical microscope objectives in both arms (a configuration known as a Linnik interferometer) [Fig. S1b]. They are again collimated by a lens (L3) of focal length f_3=200 mm. The two lenses (L2) and (L3) thus constitute a $4f$ system

which compensates the effects of diffraction between the two interferometers. The vertically polarized light (sample beam) is transmitted by a polarized beam splitter cube (PBS2), propagates through a quarter-wave plate (QWP4) before being focused in the focal plane of an immersion microscope objective (MO2, Nikon, 60×, NA=1.0). The light reflected by the sample is then collected by (MO2) and propagates again through the quarter-wave plate (QWP4). Because single scattering tends to preserve polarization, the corresponding wave-field undergoes a 90° polarization rotation and gets reflected by the beam splitter (PBS2) before being focused in the plane of the camera using the convergent lens (L4) of focal length f_4 =200 mm. The combination of this lens (L4) with the microscope objective (MO1) entails a magnification M_4 of 60.

Regarding the horizontally-polarized beam at the exit of the lens (L3), it is reflected by the beam splitter (PBS2), passes through the quarter-wave plate (QWP3) before being focused by the microscope objective (MO1) identical to (MO2). The light is then reflected by the reference mirror (M3) placed in the focal plane of MO2 before being collected again by the same microscope objective (MO2). The reflected light comes through the quarter-wave plate (QWP3). As in the other arm, the polarization of the reflected beam exhibits a 90° rotation of its polarization. The beam is now vertically polarized and transmitted by the beam splitter (PBS2), before being focused on the camera with the lens (L4).

The CMOS camera (Adimec Quartz 2A-750, 2Mpx) records the interferogram with a spatial sampling equal to δ_0 =230 nm given the magnification M4. The volume of the sample from which photons can interfere with the reference beam is called the “coherence volume". Its position is dictated by the optical path difference between the reference and sample arms. Its thickness is inversely proportional to the light spectrum bandwidth [1]:

$$\delta z_t = \frac{2\ln 2}{n\pi}\left(\frac{\lambda^2}{\Delta\lambda}\right) \tag{S1}$$

with λ the central wavelength of the light source and $\Delta\lambda$ its spectral bandwidth. In the present case, $\delta z_t \sim 10$ μm. A critical tuning of the experimental set up consists in adjusting the coherence volume with the focal plane of the microscope objective. In a volumetric sample, whose refractive index differs from that of water, the coherence volume no longer coincides with the focusing plane. This focusing defect accumulates with the transverse aberrations generated by the heterogeneities of the medium. However, it is possible to compensate for it by a fine tuning of the length of the reference arm.

The experimental procedure then consists in recording the de-scanned reflection matrix $\mathbf{D}_{\Delta\rho}(z)$ at each depth z of the sample. This latter parameter is swept by means of a motorized axial displacement of the sample carrier. The scan of the relative position $\Delta\boldsymbol{\rho}$ between the incident wave-fields in the sample and reference arms is controlled by the tilt imposed by the galvanometer (M2). For each couple $(\Delta\boldsymbol{\rho}, z)$, the CCD camera conjugated with the MO focal plane records the output intensity:

$$I_\alpha(\Delta\boldsymbol{\rho}, \boldsymbol{\rho}_{\text{out}}, z) = \int_0^T |e^{i\alpha} E_{\text{out}}(\boldsymbol{\rho}_{\text{out}}, t) + E_{\text{out}}^{(\text{ref})*}(\Delta\boldsymbol{\rho}, \boldsymbol{\rho}_{\text{out}}, t)|^2 \text{d}t \tag{S2}$$

with t the absolute time, $\mathbf{r}$ the position vector on the CCD screen, $E_{\text{out}}(\mathbf{r}, \tau)$ the scattered wave field associated with the sample arm, $E_{\text{out}}^{(\text{ref})}(\mathbf{r}, \tau)$ the reference wave field; T the integration time of the CCD camera, and α an additional phase term controlled with a piezoelectric actuator placed on mirror (M1) of the first interferometer [Fig. S1a]. The interference term is extracted from the four intensity patterns (Eq. S2) recorded at $\alpha = 0$, $\pi/2$, $3\pi/2$ and π ("four phase method" [2]):

$$D(\Delta\boldsymbol{\rho}, \boldsymbol{\rho}_{\text{out}}, z) = \frac{1}{T} \int_0^T E_{\text{out}}(\boldsymbol{\rho}_{\text{out}}, t) E_{\text{out}}^{(\text{ref})*}(\Delta\boldsymbol{\rho}, \boldsymbol{\rho}_{\text{out}}, t) \text{d}t \tag{S3}$$

As we will see in the next section, under certain conditions, this interference term tends towards the coefficients of the focused reflection matrix $\mathbf{R_{rr}}$ that would be recorded by the coherent set up displayed in Fig. S1c [Eq.1 of the accompanying article].

In particular, for $\Delta\boldsymbol{\rho} = \mathbf{0}$ (FFOCT set up), the de-scanned wave-field is equivalent to a time-gated confocal image [3]. On the one hand, the confocal nature of the recorded wave-field implies a transverse resolution $\delta\rho_0 \sim \lambda/4NA$. On the other hand, the axial resolution is either controlled by the thickness δz_t of the coherence volume or the depth-of-field δz_0 of the microscope objective: $\delta z_0 = n\lambda/NA^2$. In the present case, $\delta z_0 \sim 1$ μm$< \delta z_t \sim 10$ μm. The axial resolution is thus given by the depth-of-field. $\delta\rho_0$ and δz_0 thus dictate the values of the transverse and axial sampling of matrix $\mathbf{D}$ in our experiment.

S2. THEORETICAL EXPRESSION OF THE DE-SCANNED MATRIX

In this section, we investigate to which extent the de-scanned matrix recorded by the experimental set up in Figs. S1a,b can be considered equivalent to the focused reflection matrix that would be recorded by the fictitious coherent set up displayed in Fig. S1c.

To that aim, we will rely on the simple Fourier optics model proposed in a recent paper [3] to describe the manifestation of aberrations in FFOCT. For the sake of simplicity, this model is scalar. The large numerical aperture imposes that the recorded wave-field is associated with single scattering events taking place in the focal plane of the MO.

The wave field $E_{\text{out}}(\boldsymbol{\rho}_{\text{out}}, z)$ reflected by the sample arm in the camera plane can then be expressed as follows [3]:

$$E_{\text{out}}(\boldsymbol{\rho}_{\text{out}}, z, \omega) = \int_{\Sigma_0} \int_{\Sigma_\rho} H_{\text{out}}(\boldsymbol{\rho}_{\text{out}}, \boldsymbol{\rho}, z) \gamma(\boldsymbol{\rho}, z) H_{\text{in}}(\boldsymbol{\rho}, \boldsymbol{\rho}_0, z) E_s(\boldsymbol{\rho}_0, \omega) d\mathbf{r} d\boldsymbol{\rho}_0. \tag{S4}$$

$E_{\text{in}}(\boldsymbol{\rho}_0, \omega)$ is the incident wave-field in the secondary source plane Σ_0 at frequency ω. Light propagation between Σ_0 and the focal plane Σ_ρ is described by the impulse response $H(\boldsymbol{\rho}_0, \boldsymbol{\rho})$ between a point in the secondary source plane at transverse coordinate $\boldsymbol{\rho}_0$ and a point in the focal plane at coordinate $\boldsymbol{\rho}$. It accounts for sample-induced aberrations. $\gamma(\boldsymbol{\rho}, z)$ represents the sample reflectivity at depth z. By spatial reciprocity, the propagation of the reflected wave-field from the sample to the detector plane is also modelled by the impulse response $H(\boldsymbol{\rho}, \boldsymbol{\rho}_{\text{out}})$. The relatively narrow bandwidth ($\Delta\lambda << \lambda$) of the light source and the use of achromatic optical elements (lens, beam splitter, quarter wave plate) allows us to neglect the dependence of H on frequency ω.

Replacing $\gamma(\rho, z)$ by a uniform reflectivity in Eq. S4 and taking into account the lateral shift of the reference wave-field induced by the galvanometer M2 [Fig. S1] leads to the following previous expression for $E_{\text{out}}^{(\text{ref})}(\boldsymbol{\rho}_{\text{out}}, z)$ [3]:

$$E_{\text{out}}^{(\text{ref})}(\boldsymbol{\rho}_{\text{out}}, \Delta\boldsymbol{\rho}, z) = \int_{\Sigma_0} H_{\text{ref}}(\boldsymbol{\rho}_{\text{out}} - \boldsymbol{\rho}_0) E_0(\boldsymbol{\rho}_0 + \Delta\boldsymbol{\rho}) d\mathbf{r} d\boldsymbol{\rho}_0. \tag{S5}$$

where H_{ref} is the impulse response associated with the reference arm (way and return path) that we assume as spatially-invariant [$H_{\text{ref}}(\boldsymbol{\rho}_{\text{out}}, \boldsymbol{\rho}_0) = H_{\text{ref}}(\boldsymbol{\rho}_{\text{out}} - \boldsymbol{\rho}_0)$].

The de-scanned wave-field is obtained by extracting the interference term between the reflected wave-fields coming from the sample and reference arms:

$$D(\boldsymbol{\rho}_{\text{out}}, \Delta\boldsymbol{\rho}, z) = \langle E_{\text{out}}(\boldsymbol{\rho}_{\text{out}}, \omega) E_{\text{out}}^{(\text{ref})*}(\boldsymbol{\rho}_{\text{out}}, \omega) \rangle \tag{S6}$$

Assuming a spatially-incoherent incident wave-field $[\langle E_0(\mathbf{r}_0)E_0^*(\mathbf{r}'_0)\rangle = I_0\delta(\mathbf{r}_0 - \mathbf{r}'_0)]$ and injecting Eqs. S4 and S5 into the last equation leads to the following expression for $\mathbf{D}-$matrix coefficients:

$$D(\boldsymbol{\rho}_{\text{out}}, \Delta\boldsymbol{\rho}, z) = I_0 \iiint H(\boldsymbol{\rho}_{\text{out}}, \boldsymbol{\rho}, z)\gamma(\boldsymbol{\rho}, z)\left[H \odot H^*_{\text{ref}}\right](\boldsymbol{\rho}, \boldsymbol{\rho}_{out} + \Delta\boldsymbol{\rho}, z)d\boldsymbol{\rho} \qquad \text{(S7)}$$

where the symbol $\odot$ stands for the convolution product over the variable $\boldsymbol{\rho}_{out} + \Delta\boldsymbol{\rho}$.

The coefficients of a focused reflection matrix recorded by the fictitious coherent set up displayed in Fig. S1 can be expressed as:

$$R(\boldsymbol{\rho}_{\text{out}}, \boldsymbol{\rho}_{\text{in}}, z) = I_0 \iiint H(\boldsymbol{\rho}_{out}, \boldsymbol{\rho}, z)\gamma(\boldsymbol{\rho}, z)H(\boldsymbol{\rho}, \boldsymbol{\rho}_{in}, z)d\boldsymbol{\rho} \qquad \text{(S8)}$$

Only, a perfect reference arm would imply $\mathbf{T}_{\text{ref}} \equiv \mathbf{1}_{k<NA}$ and $H \odot H^*_{\text{ref}} \equiv H$. Equations S7 and S8 are then strictly identical in this ideal case: The incoherent set up of Fig. S1a is equivalent to the fictitious coherent set up of Fig. S1b. In reality, the reference arm can exhibit aberrations such as a slight defocus of the reference mirror M3 in Fig. S1b or a slight defocus of the reference beam in the secondary source plane at the output of first interferometer.

The comparison between Eq. S7 and Eq.2 of the accompanying paper leads to the following identification: $H_{\text{out}} \equiv H$ and $H_{\text{in}} \equiv H \odot H^*_{\text{ref}}$. In other words, while the output transmission matrices ($\mathbf{H}_{\text{out}}$, or equivalently, $\mathbf{T}_{\text{out}}$) only grasp the sample-induced aberrations, the input transmission matrices ($\mathbf{H}_{\text{in}}$ and $\mathbf{T}_{\text{in}}$) also contain the aberrations undergone by the incident and reflected reference beams. This feature explains the difference between the transmission matrices $\hat{\mathbf{T}}_{\text{in}}$ and $\hat{\mathbf{T}}_{\text{in}}$ shown in Fig.4 of the accompanying paper in which the input transmission matrix $\hat{\mathbf{T}}_{\text{in}}$ (Fig. 4e) shows an additional spherical aberration on top of the sample-induced aberrations exhibited by $\hat{\mathbf{T}}_{\text{out}}$ (Fig. 4f).

S3. MEASURING THE SCATTERING MEAN FREE PATH

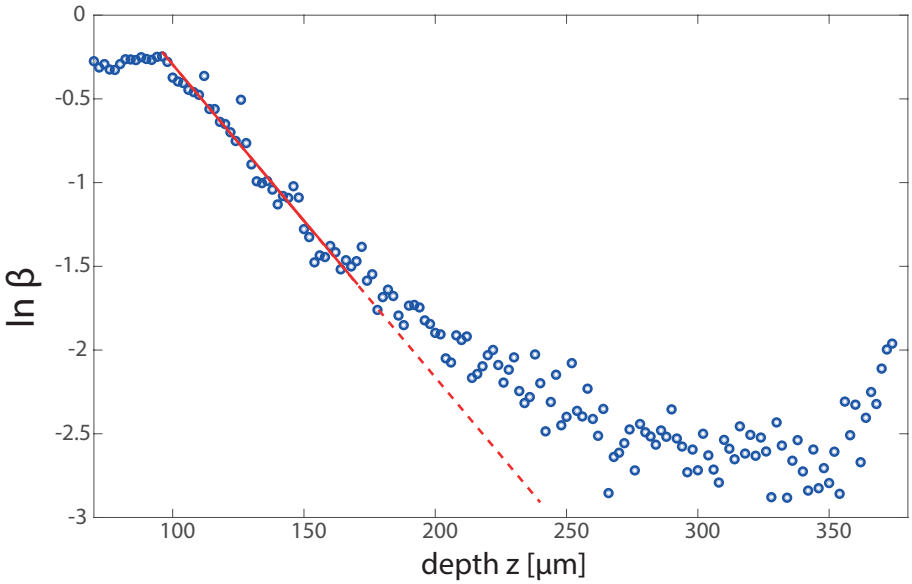

FIG. S2. Confocal scattering ratio $\ln \beta$ versus depth (blue dots) fitted with Eq. S9 (red line).

In a previous work [4], the scattering mean free path ℓ_s in the cornea has been measured by investigating the depth evolution of the confocal intensity. Indeed, in the single scattering regime, under the paraxial approximation and for an homogeneous reflectivity, the time-gated confocal intensity is supposed to decrease as $\exp(-2z/\ell_s)$ if we neglect absorption losses [5, 6].

Unfortunately, here, the cornea is not healthy but oedematous. The depth evolution of the confocal intensity in the stroma is thus strongly impacted by multiple scattering and cannot be used for a measurement of ℓ_s. Moreover, in the epithelium, the different layers of cell make the cornea reflectivity too heterogeneous to provide an exponential decrease of the confocal intensity.

Recently, an alternative strategy has been proposed in presence of multiple scattering. It consists in investigating the depth evolution of the ratio β between the confocal surintensity and the total intensity [7]. For a medium statistically homogeneous in terms of disorder, numerical simulations have shown empirically that this quantity scales as [8]:

$$\beta(z) \sim \exp(-4z/(3\ell_s) \tag{S9}$$

In the present case, this confocal ratio β has been measured as follows:

$$\hat{\beta}(z) = 1 - \frac{\min\limits_{\Delta\boldsymbol{\rho}} \{I(\Delta\boldsymbol{\rho}, z)\}}{\max\limits_{\Delta\boldsymbol{\rho}} \{I(\Delta\boldsymbol{\rho}, z)\}} \tag{S10}$$

This estimator $\hat{\beta}$ relies on the fact that the multiple scattering component of the RPSF exhibits a flat background such that it can estimated with the minimum of $I(\Delta\boldsymbol{\rho}, z)$. This hypothesis is wrong at shallow depth since the diffuse halo grows as $\sqrt{Dt}$. Nevertheless, beyond ℓ_s or so (here 100 μm), the multiple scattering background can be considered as flat as illustrated by Fig. 3d of the accompanying paper.

Figure S2 displays the depth evolution of the estimator $\hat{\beta}(z)$. It exhibits an exponential decay in the stroma beyond $z = 100$ μm. The decay rate decreases beyond $z = 170$ μm because our estimator of $\beta(z)$ starts to be impacted by the experimental noise [see Fig. 3d of the accompanying paper]. Therefore, the fit of $\hat{\beta}(z)$ with Eq. S9 is performed from $z = 100$ to $z = 170$ μm. We find $\ell_s \sim 70$ μm.

S4. THEORETICAL EXPRESSION OF THE CORRELATION MATRIX

The multi-scale analysis of $\mathbf{D}$ allows an estimation of the $\mathbf{T}-$matrix at an increasingly finer resolution, by iteratively reducing the area over which each aberration phase law is estimated. At each step, the iterative phase reversal (IPR) algorithm assumes the convergence of the correlation matrix $\mathbf{C}(\mathbf{r}_p)$ (Eq.8) towards its ensemble average $\langle \mathbf{C} \rangle (\mathbf{r}_p)$, the so-called covariance matrix [9, 10]. In fact, this convergence is never fully realized and $\mathbf{C}$ should be decomposed as the sum of this covariance matrix $\langle \mathbf{C} \rangle (\mathbf{r}_p)$ and a perturbation term $\delta\mathbf{C}(\mathbf{r}_p)$:

$$\mathbf{C}(\mathbf{r}_p) = \langle \mathbf{C} \rangle (\mathbf{r}_p) + \delta\mathbf{C}(\mathbf{r}_p). \tag{S11}$$

The intensity of the perturbation term scales as the inverse of the number $N_{\mathrm{L}} = (L/\delta_0)^2$ of resolution cells in each sub-region [10, 11]:

$$\left\langle |\delta C(\mathbf{u}, \mathbf{u}', \mathbf{r}_p)|^2 \right\rangle = \frac{\left\langle |C(\mathbf{u}, \mathbf{u}', \mathbf{r}_p)|^2 \right\rangle}{N_L} \tag{S12}$$

This perturbation term can thus be reduced by increasing the size L of the spatial window W_L, but at the cost of a resolution loss. In the following, we express theoretically the bias induced by this perturbation term on the estimation of $\mathbf{T}$. In particular, we will show how it scales with the parameter L and the focusing quality. To that aim, we will consider the input correlation matrix $\mathbf{C}_{\mathrm{in}}$ but a similar demonstration can be performed at output. For sake of lighter notation, the dependence over $\mathbf{r}_p$ will be omitted in the following.

Under assumptions of local isoplanicity and random reflectivity, the covariance matrix can be expressed as follows [9]:

$$\langle \mathbf{C}_{\mathrm{in}} \rangle = \mathbf{T}_{\mathrm{in}} \times \mathbf{C}_H \times \mathbf{T}_{\mathrm{in}}^{\dagger}, \tag{S13}$$

or in terms of matrix coefficients,

$$\langle \mathbf{C}_{\mathrm{in}} \rangle (\mathbf{u}, \mathbf{u}') = T_{\mathrm{in}}(\mathbf{u}) T_{\mathrm{in}}^{*}(\mathbf{u}') \underbrace{\int d\boldsymbol{\rho} |H_{\mathrm{out}}(\boldsymbol{\rho})|^2 e^{-i2\pi \frac{(\mathbf{u}-\mathbf{u}').\rho}{\lambda f}}}_{=C_H(\mathbf{u},\mathbf{u}')}. \tag{S14}$$

$\mathbf{C}_H$ is a reference correlation matrix associated with a virtual reflector whose scattering distribution corresponds to the output focal spot intensity $|H_{\mathrm{out}}(\boldsymbol{\rho})|^2$. This scatterer plays the role of virtual guide star in the RMI process.

S5. ESTIMATION OF THE T−MATRIX

For such an experimental configuration, an iterative time reversal process converges towards a wavefront that maximizes the energy back-scattered by the reflector [12, 13]. Mathematically, this iterative time reversal process writes as follows

$$\mathbf{U}_{\text{in}}^{(n+1)} = \sigma \mathbf{C}_{\text{in}} \times \mathbf{U}_{\text{in}}^{(n)} \tag{S15}$$

with $\mathbf{U}_{\text{in}}^{(n)}$, the wave-front at iteration n of the iterative time reversal process and σ, the scatterer reflectivity. Iterative time reversal converges towards a wave front, $\mathbf{U}_{\text{in}} = \lim_{n\to+\infty} \mathbf{U}_{\text{in}}^{(n)}$, that is none other than the first eigenvector of $\mathbf{C}_{\text{in}}$.

If the virtual reflector was point-like, this wave-front would be a perfect estimator of $\mathbf{T}_{\text{in}}$. Its phase conjugate perfectly compensates for aberrations and focuses through the heterogeneous medium onto the point-like target [12, 13]. However, here the virtual guide star is enlarged compared to the diffraction limit. Iterative time reversal thus converges towards a wave-front $\mathbf{U}_{\text{in}}$ of finite angular support δu_c that tends to focus on the center of the virtual reflector but with a resolution width $\delta\rho_c \sim \lambda f/\delta u_c$ larger than the diffraction limit [10].

To circumvent that issue, the iterative phase reversal algorithm has been developed. It consists in modifying the iterative time reversal process as follows:

$$\hat{\mathbf{T}}_{\text{in}}^{(n+1)} = \exp\left[i \arg\left\{\mathbf{C}_{\text{in}} \times \hat{\mathbf{T}}_{\text{in}}^{(n)}\right\}\right] \tag{S16}$$

where $\hat{\mathbf{T}}_{\text{in}}^{(n)}$ is the estimator of $\mathbf{T}_{\text{in}}$ at the n^{th} iteration of the phase reversal process. $\hat{\mathbf{T}}_{\text{in}}^{(0)}$ is an arbitrary wave-front that initiates the iterative phase reversal process (typically a flat phase law). $\hat{\mathbf{T}}_{\text{in}} = \lim_{n\to\infty} \hat{\mathbf{T}}_{\text{in}}^{(n)}$ is the result of this iterative phase reversal process. The iterative phase reversal algorithm differs from an iterative time reversal process by imposing the $\mathbf{T}$-matrix coefficients to be of constant modulus in the pupil plane. In other words, unlike the iterative time reversal process, the resulting wave-front here equally addresses each angular component of the imaging process to reach a diffraction-limited resolution. While the iterative time reversal process is guided by a maximization of the back-scattered energy, the iterative phase reversal process is dictated by a minimization of the resolution length.

In practice, however, the $\mathbf{T}-$matrix estimator is still impacted by the blurring of the synthesized guide star and the presence of diffusive background and/or noise. Therefore the

whole process shall be iterated at input and output in order to gradually refine the guide star and reduce the bias on our $\mathbf{T}-$matrix estimator. Moreover, the spatial window W_L over which the $\mathbf{C}-$matrix is computed [Eq. 8 in the accompanying paper] shall be gradually decreased in order to address the forward multiple scattering component, the latter one being associated with smaller isoplanatic patches.

To understand the parameters controlling the bias $\delta\hat{\mathbf{T}}_{\rm in}$ between $\hat{\mathbf{T}}_{\rm in}$ and $\mathbf{T}_{\rm in}$, one can express $\hat{\mathbf{T}}_{\rm in}$ as follows:

$$\hat{\mathbf{T}}_{\rm in} = \exp\left(j\arg\left\{\mathbf{C}_{\rm in}\times\hat{\mathbf{T}}_{\rm in}\right\}\right) = \frac{\mathbf{C}_{\rm in}\times\hat{\mathbf{T}}_{\rm in}}{||\mathbf{C}_{\rm in}\times\hat{\mathbf{T}}_{\rm in}||} \tag{S17}$$

By injecting Eq. S11 into the last expression, $\hat{\mathbf{T}}_{\rm in}$ can be expressed, at first order, as the sum of its expected value $\mathbf{T}_{\rm in}$ and a perturbation term $\delta\hat{\mathbf{T}}_{\rm in}$:

$$\hat{\mathbf{T}}_{\rm in} = \underbrace{\frac{\langle\mathbf{C}_{\rm in}\rangle\times\mathbf{T}_{\rm in}}{||\langle\mathbf{C}_{\rm in}\rangle\times\mathbf{T}_{\rm in}||}}_{=\mathbf{T}_{\rm in}} + \underbrace{\frac{\delta\mathbf{C}_{\rm in}\times\mathbf{T}_{\rm in}}{||\langle\mathbf{C}_{\rm in}\rangle\times\mathbf{T}_{\rm in}||}}_{\simeq\delta\hat{\mathbf{T}}_{\rm in}}. \tag{S18}$$

The bias intensity can be expressed as follows:

$$||\delta\hat{\mathbf{T}}_{\rm in}||^2 = \frac{\mathbf{T}_{\rm in}^\dagger\times\delta\mathbf{C}_{\rm in}^\dagger\times\delta\mathbf{C}_{\rm in}\times\mathbf{T}_{\rm in}}{\mathbf{T}_{\rm in}^\dagger\times\langle\mathbf{C}_{\rm in}\rangle^\dagger\times\langle\mathbf{C}_{\rm in}\rangle\times\mathbf{T}_{\rm in}} \tag{S19}$$

Using Eq. S12, the numerator of the previous equation can be expressed as follows:

$$\mathbf{T}_{\rm in}^\dagger\times\delta\mathbf{C}_{\rm in}^\dagger\times\delta\mathbf{C}_{\rm in}\times\mathbf{T}_{\rm in} = M^2\delta u_0^2\langle|\delta C_{\rm in}(\mathbf{u},\mathbf{u}')|^2\rangle = M^2\delta u_0^2\langle|\langle C_{\rm in}\rangle(\mathbf{u},\mathbf{u})|^2\rangle/N_L. \tag{S20}$$

with $\delta u_0\sim\lambda f/\delta_R$, the resolution of the $\mathbf{T}-$matrix in the pupil plane and δ_R, the de-scan field-of-view. Injecting Eq. S14 into the last equation leads to the following expression for the numerator of Eq. S19:

$$\mathbf{T}_{\rm in}^\dagger\times\delta\mathbf{C}_{\rm in}^\dagger\times\delta\mathbf{C}_{\rm in}\times\mathbf{T}_{\rm in} = M^2\delta u_0^2\left|T_{\rm out}\overset{\mathbf{u}_{\rm out}}{\circledast}T_{\rm out}(\mathbf{0})\right|^2/N_{\rm L}. \tag{S21}$$

The denominator of Eq. S19 can be expressed as follows:

$$\mathbf{T}_{\rm in}^\dagger\times\langle\mathbf{C}_{\rm in}\rangle^\dagger\times\langle\mathbf{C}_{\rm in}\rangle\times\mathbf{T}_{\rm in} = M^2\left|\sum_{\mathbf{u}}T_{\rm out}\overset{\mathbf{u}_{\rm out}}{\circledast}T_{\rm out}(\mathbf{u})\right|^2 \tag{S22}$$

The bias intensity is thus given by:

$$||\delta\hat{\mathbf{T}}_{\rm in}||^2 = \frac{\delta u_0^2\left|T_{\rm out}\overset{\mathbf{u}_{\rm out}}{\circledast}T_{\rm out}(\mathbf{0})\right|^2}{\left|\sum_{\mathbf{u}}T_{\rm out}\overset{\mathbf{u}_{\rm out}}{\circledast}T_{\rm out}(\mathbf{u})\right|^2} = \frac{\delta_R^{-2}\int d\mathbf{r}|H_{\rm out}(\mathbf{r})|^2}{|H_{\rm out}(\mathbf{r}=\mathbf{0})|^2} \tag{S23}$$

The bias thus scales as the ratio between the mean incoherent input intensity and the coherent intensity (energy deposited exactly at focus). It is thus inversely proportional to the focusing quality at output. In terms of order of magnitude, we have $\left|\sum_{\mathbf{u}} T_{\text{out}} \overset{\mathbf{u}_{\text{out}}}{\circledast} T_{\text{out}}(\mathbf{u})\right|^2 \sim \delta u_{\text{out}}^2 \left|T_{\text{out}} \overset{\mathbf{u}_{\text{out}}}{\circledast} T_{\text{out}}(\mathbf{0})\right|^2$, with $\delta u_{\text{out}} \sim \lambda f/\delta r_{\text{out}}$ the coherence length of the $\mathbf{T}-$matrix in the output pupil plane and δr_{out}, the spatial extension of the output PSF. The bias intensity thus exhibits the following scaling law,

$$||\delta\hat{\mathbf{T}}_{\text{in}}||^2 \sim \frac{D_{\text{out}}}{MN_{\text{L}}}. \tag{S24}$$

where $D_{\text{out}} = (\delta r_{\text{out}}/\delta_0)^2$ is the characteristic size of the output focal spot in terms of resolution cells.

This last expression justifies the multi-scale analysis proposed in the accompanying paper. A gradual decrease of the aberration level, quantified by D_{out}, is required to address smaller spatial windows that scale as N_{L}. Following this scheme, the bias of the $\mathbf{T}-$matrix can be minimized and the iterative phase reversal algorithm converges towards a satisfying estimator.

However, the spatial window cannot be reduced to a speckle grain otherwise the method would lead to a bucket image that consists in an incoherent summation of each de-scanned wave-field. Figure S3c illustrates this fact by displaying the en-face image obtained when the spatial window reaches a size $L = 3$ μm. Compared with $L = 6$ μm [Figure S3b], the image has clearly lost some contrast, which is a manifestation of an incoherent compensation of aberrations and scattering (bucket image).

The iteration should therefore be stopped at some point. In practice, the end of the process can be determined by a careful look at the image. An incoherent compensation of aberrations induces a loss of contrast on the final image. Figure S3 illustrates those detrimental effects by comparing the original image (Fig. S3a), the RMI image obtained with a $\mathbf{T}-$matrix of optimal resolution (6×6 μm^2, see Fig. S3b) and a RMI image relying on too small spatial windows W_L (3×3 μm^2, see Fig. S3c). The contrast of each image $I(\boldsymbol{\rho}, z)$, $\mathcal{C}(z) = \text{std}\left[I(\boldsymbol{\rho}, z)\right] / \left\langle I(\boldsymbol{\rho}, z)\right\rangle$, tends to gradually increase when the estimator $\hat{\mathbf{T}}$ approaches $\mathbf{T}$ (see comparison between Figs. S3a and b) and decrease when the compensation of aberrations and scattering becomes bucket-like (see comparison between Figs. S3b and c). For the images displayed in Figs. S3a, b and c, we find $\mathcal{C} \sim 1.48$, $\mathcal{C} \sim 1.61$ and $\mathcal{C} \sim 1.37$, respectively. Nevertheless, an optimization criterion only based on the image contrast can be misleading since the contrast also depends on the sample reflectivity distribution.

A more reliable observable is the spatial correlation of the $\mathbf{T}$-matrix between neighbor patches as displayed in Fig.6e of the accompanying paper. While a spatial window of 6×6 μm^2 preserves a short-range correlation between neighbor windows (see inset of Fig. S3b), a spatial window of 3×3 μm^2 leads to a fully spatially incoherent estimator $\hat{\mathbf{T}}$ (see inset of Fig. S3c). This observable clearly shows whether the estimator $\hat{\mathbf{T}}$ leads to a coherent (i.e physical) or incoherent (i.e bucket-like) compensation of multiple scattering. The number of iterations in the phase reversal algorithm has thus been based on this $\mathbf{T}$-matrix correlation criterion.

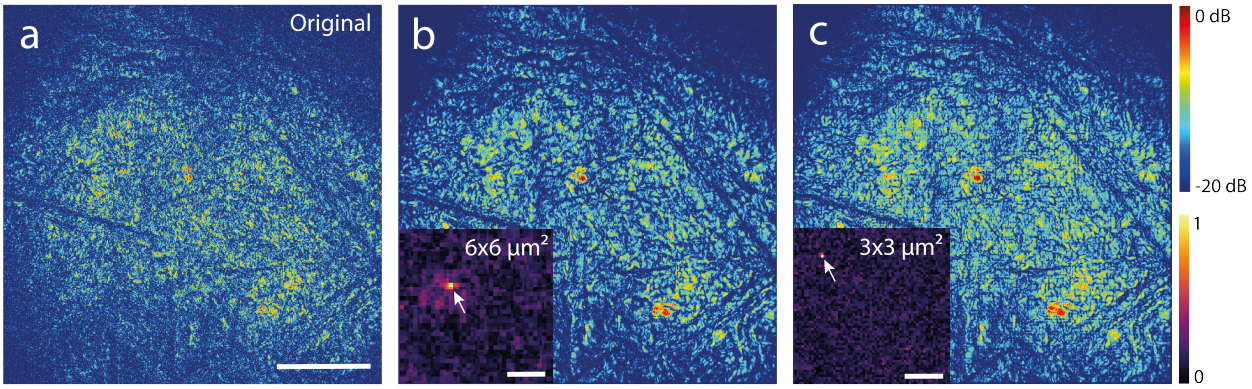

FIG. S3. **Confocal images at several steps of the multi-scale analysis**. **a** Initial en-face image of the cornea at depth $z \sim 100$ μm. **b** RMI image based on a $\mathbf{T}$-matrix estimator of spatial resolution $L = 6$ μm. **c** RMI image based on a $\mathbf{T}$-matrix estimator of spatial resolution $L = 3$ μm. The spatial correlation of $\hat{\mathbf{T}}$ with respect to one reference location (white arrow) is displayed in insets of panels b and c. Scale bars : 50 μm.

S6. QUANTIFYING THE CONTRAST ENHANCEMENT

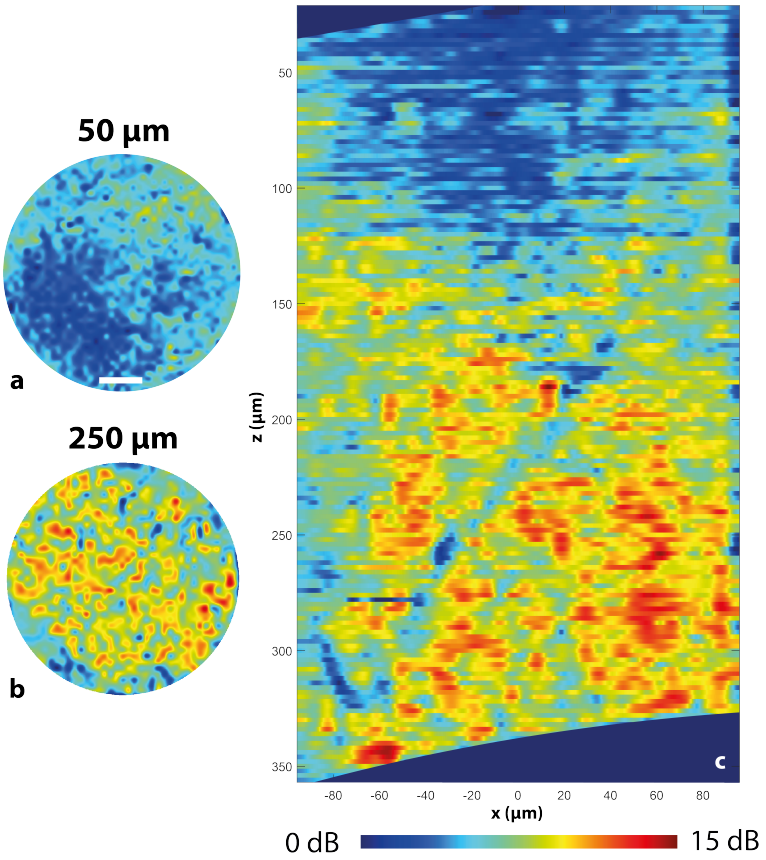

FIG. S4. **Confocal gain provided by the matrix imaging process**. **ab.** Transverse cross-section of the confocal gain observed for the *en-face* images displayed in Fig. 3b at depths 50 μm and 250 μm within the cornea [scale bar: 50 μm]. **c.** Longitudinal cross-section of the confocal gain observed by comparing the B-scan displayed in Fig.3f with its original version shown in Fig. 3c. In each panel, the color scale is in dB.

Figure S4 shows the enhancement of the confocal peak before and after RMI. It reaches a maximal value of 30. This gain should scale, in amplitude, as the number P_c of independent coherence grains exhibited by the $\mathbf{T}-$matrix in the pupil plane (see, for instance, Figs. 4e and f) and that RMI tends to realign in phase by means of a digital optical phase conjugation. Figure S4b clearly shows that the confocal gain increases with depth z. Indeed, multiple scattering becomes predominant in depth and the transmission phase laws become more and more complex. Note, however, that given the complexity of phase laws displayed in Figs. 4e and f, we could have expected a larger confocal intensity enhancement. This moderate gain

in contrast is explained by the fact that a part of the multiple scattering background is not addressed by RMI.

[1] A. F. Fercher, J. Biomed. Opt. **1**, 157 (1996).

[2] A. Badon, D. Li, G. Lerosey, A. Claude Boccara, M. Fink, and A. Aubry, Optica **3**, 1160 (2016).

[3] V. Barolle, J. Scholler, P. Mecê, J.-M. Chassot, K. Groux, M. Fink, A. C. Boccara, and A. Aubry, Opt. Express **29**, 22044 (2021).

[4] R. Bocheux, P. Pernot, V. Borderie, K. Plamann, and K. Irsch, PLOS ONE **14**, e0221707 (2019).

[5] A. Badon, A. C. Boccara, G. Lerosey, M. Fink, and A. Aubry, Opt. Express **25**, 28914 (2017).

[6] U. Tricoli and R. Carminati, J. Opt. Soc. Am. A **36**, C122 (2019).

[7] C. Brütt, A. Aubry, B. Gérardin, A. Derode, and C. Prada, Phys. Rev. E **106**, 025001 (2022).

[8] A. Goicoechea, C. Brutt, F. Bureau, A. Le Ber, C. Prada, and A. Aubry, to be submitted (2023).

[9] W. Lambert, L. A. Cobus, T. Frappart, M. Fink, and A. Aubry, Proc. Natl. Acad. Sci. U. S. A. **117**, 14645 (2020).

[10] W. Lambert, L. A. Cobus, J. Robin, M. Fink, and A. Aubry, IEEE Trans. Med. Imag. **41**, 3921 (2022).

[11] J.-L. Robert and M. Fink, J. Acoust. Soc. Am. **123**, 866 (2008).

[12] C. Prada and M. Fink, Wave Motion **20**, 151 (1994).

[13] C. Prada, S. Manneville, D. Spoliansky, and M. Fink, J. Acoust. Soc. Am. **99**, 2067 (1996).